Two-dimensional sparse fractional Fourier transform and its applications

Deyun Wei*, Jun Yang

School of Mathematics and Statistics, Xidian University, Xi'an 710071, PR China

ARTICLE INFO

ABSTRACT

The discrete fractional Fourier transform is an excellent tool in non-stationary signal processing. And an efficient and accurate computation is important for the two-dimensional discrete fractional Fourier transform (2D DFRFT). Inspired by the sparse Fourier transform algorithm, we propose a two-dimensional sparse fractional Fourier transform (2D SFRFT) algorithm to estimate the fractional Fourier spectrum efficiently. Compared with existing methods, we have achieved the lowest runtime and sample complexity. Moreover, by analyzing the errors due to noises, the 2D SFRFT algorithm is improved to be robust. The applications in image fusion, parameter estimation of multicomponent 2D chirp signal and complex maneuvering targets in SAR radar demonstrate the effectiveness of the proposed algorithms.

1. Introduction

The Fourier transform (FT) is an important tool in communication, signal processing, and other fields [1–4]. However, for non-stationary signals, the FT cannot analyze their time-frequency characteristics completely. The non-stationary signals, especially the chirp signals, are common in radar [5,6], gravitational waves [7], etc. As a generalized FT, the fractional Fourier transform (FRFT) [8–11] has the advantage of processing non-stationary signals [12–15]. It decomposes the signals by chirp orthonormal basis instead of sine basis, and the chirp signals are energy aggregated in the FRFT domain. The FRFT has been applied to optical systems [16], communication [17], signal and image processing [18–20], and other fields [21–24] successfully.

Efficiently numerical algorithms for FRFT are necessary for engineering. Many definitions [25–31] of discrete fractional Fourier transform (DFRFT) have been proposed and can be classified as sampled DFRFT, eigendecomposition DFRFT, and linearly weighted DFRFT. The linearly weighted DFRFT is used rarely since it cannot approximate the continuous FRFT. The eigendecomposition DFRFT is not closed and there is no effective fast algorithm. So, it is difficult to be used in real-time engineering. For applications that do not require rotational additivity, the sampled DFRFT is

the favorite and corresponding fast algorithms [30–37] are studied. Pei [31] proposes currently the most efficient definition of DFRFT with the runtime complexity $O(N \log N)$. Based on Pei-type DFRFT and the sparse nature of some real signals, Liu [32] proposes the SFRFT algorithm and reduces the runtime complexity to $O(N + \sqrt{kN \log N} \log N)$. Where k denotes the signals' sparsity. Subsequently, variants of SFRFT are investigated and applied to radar [33–36]. However, the study of SFRFT is limited to one dimension. The two-dimensional (2D) DFRFT [38] is important and more computational. Thus, fast algorithms for 2D DFRFT are needed.

Based on the advantages of FRFT, 2D DFRFT has been applied to image processing [39–43], remote sensing [44], radar [18], artificial intelligence [45], and so on. However, little literature is devoted to the efficient implementation of 2D DFRFT. Generally, the 2D DFRFT is obtained by cascading the 1D DFRFT of the rows and columns of the signal. Utilizing the fast algorithm of 1D DFRFT, the runtime complexity of 2D DFRFT is $N_1 + N_2$ times that of 1D DFRFT. It is worth noting that SFRFT requires the signal to be sparse after the transformation. Thus, the SFRFT algorithm with low runtime complexity cannot replace two sets of 1D DFRFTs. To summarize, 2D DFRFT is time-consuming. Moreover, all discrete points of the signal are used, making data acquisition, storage, and transmission challenges. It is necessary to study the SFRFT algorithm for two dimensions signals.

With low computational and sampling costs, the SFT [46–50] are efficient algorithms to estimate the discrete Fourier transform (DFT). And the 2D SFT algorithms [51–56] are proposed. Among them, the downsampled method [51] performs only a few 1D DFTs. The algorithm has a simple structure and low complexity

for noiseless signals. However, it may be locked if the signals are not appropriate. To address this limitation, different schemes [52–54] are investigated. And by randomly downsampled slices, the algorithm in Wang et al. [54] has the strongest degree of freedom and the lowest runtime complexity. Moreover, the sparsity does not have to be pre-given, which fits the real applications. However, 2D SFT cannot be used for non-stationary signals. Therefore, we are willing to propose algorithms to estimate the 2D DFRFT based on sparsity and randomly downsampled slices. In addition, for the case of noise, the voting method in Wang et al. [54] is only suitable for high SNR. We expect to extend the range of SNR in the novel algorithm estimating 2D DFRFT.

To estimate 2D DFRFT with low sample and runtime complexity, we will propose a two-dimensional sparse fractional Fourier transform (2D SFRFT) algorithm. The signals' 2D FRFT domain are assumed to be sparse, which is common in radar, magnetic resonance images, optical images, and other engineering. The 2D SFRFT algorithm will be implemented by chirp products and downsampled 2D SFT. The sparsity can be unknown and only a few slices of data will be leveraged. Thus the 2D SFRFT algorithm can achieve an unprecedented low sample and runtime complexity. The localization errors caused by noises will be analyzed and the significant frequency position estimation method of the 2D DFRFT algorithm will be improved to robust. The robust 2D SFRFT algorithm can achieve 2D DFRFT estimation at low SNR with great probability. The specific contributions of this paper are as follows.

- Firstly, based on the Pei-type DFRFT, a definition of 2D DFRFT is given, which is the target to be estimated.
- Secondly, based on randomly downsampled slices, we establish the 2D SFRFT algorithm for noiseless signals. The 2D DFRFT can be fully estimated with sample complexity $O(T)$ and runtime complexity $O(L \log L + k)$. Where $L = LCM(N_1, N_2)$ and T is the number of iterations.
- Thirdly, we analyze the effect of noises on the 2D SFRFT and upgrade 2D SFRFT to be robust. With s inner loops, the sample and runtime complexity are $O(L(T + sk))$, $O((T + sk)L \log L)$, respectively. The correctly estimated probabilities are also analyzed.
- Finally, we verify the performance and convergence of the proposed algorithms by simulation. Multi-component 2D chirp signal parameter estimation is achieved and precision is far superior to that of 2D SFT. In addition, the robust 2D SFRFT algorithm is applied to image fusion and SAR radar successfully.

The rest of this paper is organized as follows. Section 2 describes the definition of Pei-type DFRFT and 2D DFRFT. In Section 3, the 2D SFRFT algorithm is introduced. Robust improvements are provided in Section 4. The relevant simulations and applications are presented in Sections 5 and 6. Section 7 concludes the paper.

2. Preliminaries

In this section, we will describe the definition of the Pei-type DFRFT and 2D DFRFT.

2.1. The closed-form discrete fractional Fourier transform

The continuous fractional Fourier transform (FRFT) [8] of the signal $x(t)$ is defined as (1),

$$X_\alpha(u) = \begin{cases} \int_{-\infty}^{\infty} K_\alpha(u,t)x(t)dt & \alpha \neq c\pi \\ x(t) & \alpha = 2c\pi \\ x(-t) & \alpha = (2c+1)\pi \end{cases} \quad (1)$$

where c can be any integer. α represents the fractional order. u denotes the frequency in the fractional Fourier domain. $K_\alpha(u,t)$ is

the kernel function of FRFT, which is defined as follows

$$K_\alpha(u,t) = \sqrt{\frac{1 - j \cot \alpha}{2}} e^{\frac{j}{2}(u^2 \cot \alpha - 2ut \csc \alpha + t^2 \cot \alpha)}. \quad (2)$$

By discretizing the input and output variables directly, Pei defines an invertible discrete kernel function [31],

$$K_\alpha(m,n) = \sqrt{\frac{\text{sgn}(\sin \alpha)(\sin \alpha - j \cot \alpha)}{M}}$$
$$e^{\frac{j}{2}(m^2 \Delta u^2 \cot \alpha - \frac{2}{M} 2\pi mn \text{sgn}(\sin \alpha) + n^2 \Delta t^2 \cot \alpha)} \quad (3)$$

where $n = 0, 1, \ldots, N$ and $m = 0, 1, \ldots, M$. $sgn()$ is the symbolic function. N, M represent the number of sampling points in the time domain and fractional Fourier domain, respectively. $\Delta t, \Delta u$ denote the sampling interval in the time domain and fractional Fourier domain, respectively. Therefore, the DFRFT of discrete signal $f(n) = x(n\Delta t)$ is expressed as (4), where, constraints $M \geq N$ and (5) are restricted to ensure unity.

$$\hat{F}_\alpha(m) = \begin{cases} \sqrt{\frac{\sin \alpha - j \cos \alpha}{M}} e^{\frac{j}{2} \cot \alpha m^2 \Delta u^2} \sum_{n=0}^{N-1} e^{-j \frac{2\pi mn}{M}} e^{\frac{j}{2} \cot \alpha n^2 \Delta t^2} f(n) & \sin \alpha > 0 \\ \sqrt{\frac{-\sin \alpha + j \cos \alpha}{M}} e^{\frac{j}{2} \cot \alpha m^2 \Delta u^2} \sum_{n=0}^{N-1} e^{j \frac{2\pi mn}{M}} e^{\frac{j}{2} \cot \alpha n^2 \Delta t^2} f(n) & \sin \alpha < 0 \\ f(m) & \alpha = 2c\pi \\ f(-m) & \alpha = (2c+1)\pi \end{cases}$$

$$(4)$$

$$\Delta t \Delta u = \frac{2\pi |\sin \alpha|}{M} \quad (5)$$

For simplicity, only the case of $M = N$ is discussed. This discrete form is closed, reversible, and periodic. It can approximate the FRFT well. Although rotational additivity is not satisfied, DFRFT with α can be represented by DFRFT with β. Computationally, this transform can be decomposed into two times of multiplication with chirp signals and one FFT operation.

2.2. Two-dimensional discrete fractional Fourier transform

The 2D DFRFT [38] of (N_1, N_2)-point signal $f(s,t)$ is defined as (6), where $u = 0, 1, \ldots, M_1 - 1$, and $v = 0, 1, \ldots, M_2 - 1$. Meanwhile, N_1, N_2, M_1, M_2 are integers. M_1, M_2 represent the number of samples in the fractional Fourier domain. $K_{\alpha,\beta}(u,v,s,t)$ is the 2D separable DFRFT kernel, which is given by (7). And $\otimes$ denotes the tensor product. $K_\alpha(u,s)$ and $K_\beta(v,t)$ represent the 1D DFRFT kernel with rotation angles α and β in two dimensions, respectively.

$$\hat{F}_{\alpha,\beta}(u,v) = \sum_{s=0}^{N_1-1} \sum_{t=0}^{N_2-1} K_{\alpha,\beta}(u,v,s,t)f(s,t) \quad (6)$$

$$K_{\alpha,\beta}(u,v,s,t) = K_\alpha(u,s) \otimes K_\beta(v,t) \quad (7)$$

We only consider $\alpha > 0, \beta > 0$ and other cases are similar.

3. Proposed 2D SFRFT algorithm

In this section, we will present the two-dimensional sparse fractional Fourier transform (2D SFRFT) algorithm for a noiseless situation [61]. It will reduce the runtime and sample complexity when signals are sparse in the fractional Fourier domain.

Based on the Pei-type DFRFT, the 2D DFRFT of (N_1, N_2)-point signal $f(s,t)$ is defined as (8)

$$\hat{F}_{\alpha,\beta}(u,v) = \sqrt{\frac{(\sin \alpha - j \cos \alpha)(\sin \beta - j \cos \beta)}{M_1 M_2}} e^{j \frac{u^2 \Delta u^2}{2 \tan \alpha} + j \frac{v^2 \Delta v^2}{2 \tan \beta}}$$
$$\sum_{s=0}^{N_1-1} \sum_{t=0}^{N_2-2} f(s,t) e^{j \frac{t^2 \Delta t^2}{2 \tan \beta} + \frac{s^2 \Delta s^2}{2 \tan \alpha}} e^{-j 2\pi \left(\frac{su}{N_1} + \frac{tv}{N_2} \right)} \quad (8)$$

if $\sin\alpha > 0$ and $\sin\beta > 0$. For $\sin\alpha < 0$ and $\sin\beta < 0$, the 2D DFRFT of signal $f(s,t)$ is equal to (9),

$$\hat{F}_{\alpha,\beta}(u,v) = \sqrt{\frac{(\sin\alpha - j\cos\alpha)(\sin\beta - j\cos\beta)}{M_1 M_2}} e^{j\frac{u^2 \Delta u^2}{2\tan\alpha} + j\frac{v^2 \Delta v^2}{2\tan\beta}}$$
$$\times \sum_{s=0}^{N_1-1} \sum_{t=0}^{N_2-2} f(s,t) e^{j\frac{t^2 \Delta t^2}{2\tan\beta} + \frac{s^2 \Delta s^2}{2\tan\alpha}} e^{j2\pi\left(\frac{su}{N_1} + \frac{tv}{N_2}\right)} \quad (9)$$

where $\Delta s, \Delta t, \Delta u, \Delta v$ denote the sampling interval of the two dimensions of the time domain and fractional Fourier domain, respectively. For simplicity, only the case of $M_1 = N_1, M_2 = N_2$ is discussed. And constraints are as follows.

$$\Delta s \Delta u = \frac{2\pi |\sin\alpha|}{M_1} \quad (10)$$

$$\Delta t \Delta v = \frac{2\pi |\sin\beta|}{M_2} \quad (11)$$

When signal $f(s,t)$ is sparse in the fractional Fourier domain, the main idea of 2D SFRFT is iteration. Each iteration first subtracts the effect of the previous estimate and then estimates the nonzero frequencies. Randomly downsampled slices are used for bucketing, and the phase difference is used to estimate non-negligible frequencies. The detailed flow of the proposed 2D SFRFT algorithm is as follows:

Step 1: Multiply the original signal $f(s,t)$ with a chirp function.

$$x(s,t) = f(s,t) e^{j\frac{s^2 \Delta s^2}{2\tan\alpha} + j\frac{t^2 \Delta t^2}{2\tan\beta}} \quad (12)$$

Where $s = 0,1,\ldots,N_1 - 1$ and $t = 0,1,\ldots,N_2 - 1$. $\Delta s, \Delta t$ are the sampling interval of the two dimensions. α, β are real numbers representing fractional orders of the two dimensions. Since $f(s,t)$ is sparse in the fractional Fourier domain, $x(s,t)$ is sparse in the Fourier domain. It is supposed that the values $A_{(m_1,m_2)}$ and locations (m_1, m_2) of all non-negligible frequency points of $x(s,t)$ are stored in the set $\Omega = (A_{(m_1,m_2)}, m_1, m_2)$. In other words, suppose

$$x(s,t) = \frac{1}{N} \sum_{\Omega} A_{(m_1,m_2)} e^{j2\pi\left[\frac{m_1 s}{N_1} + \frac{m_2 t}{N_2}\right]} \quad (13)$$

where $N = N_1 N_2$. And $\Omega = (A_{(m_1,m_2)}, m_1, m_2)$ is to be estimated.

Step 2: Choose random integers $\sigma_1, \sigma_2, \tau_1, \tau_2$, where $0 \le \sigma_1, \tau_1 < N_1$ and $0 \le \sigma_2, \tau_2 < N_2$. Let the least common multiple of N_1 and N_2 be L ($L = LCM(N_1, N_2)$). Parameters must also be satisfied that (σ_1, σ_2), $(\sigma_1, \frac{L}{N_2})$, and $(\sigma_2, \frac{L}{N_1})$ are coprime pairs. This can be achieved through Algorithm 1,

---

Algorithm 1 Get algorithm.

Require: Signal sizes (N_1, N_2).
Ensure: σ_1, σ_2.
1: $L = LCM(N_1, N_2)$
2: Choose σ_1 from $0 \to N_1 - 1$ randomly
3: Choose σ_2 from $0 \to N_2 - 1$ randomly
4: **while** $g(\sigma_1, \sigma_2) \neq 1 || g(\sigma_1, \frac{L}{N_2}) \neq 1 || g(\sigma_2, \frac{L}{N_1}) \neq 1$ **do**
5:     Choose σ_1 from $0 \to N_1 - 1$ randomly
6:     Choose σ_2 from $0 \to N_2 - 1$ randomly
7: **end while**

---

where $g(a,b)$ denotes the least common multiple of a and b. If $\sin\alpha > 0, \sin\beta > 0$, extract slices $q_{\sigma_1,\sigma_2,\tau_1,\tau_2}(l)$, $q_{\sigma_1,\sigma_2,\tau_1+1,\tau_2}(l)$, $q_{\sigma_1,\sigma_2,\tau_1,\tau_2+1}(l)$ in matrix $x(s,t)$ and compute their DFT by FFT, where

$$q_{\sigma_1,\sigma_2,\tau_1,\tau_2}(l) = x([\sigma_1 l + \tau_1]_{N_1}, [\sigma_2 l + \tau_2]_{N_2}) \quad (14)$$

and $[a]_b$ means a modulo b, $l = 0,1,\ldots,L-1$. By definition, the corresponding DFT can be expressed as (15),

$$Q_{\sigma_1,\sigma_2,\tau_1,\tau_2}(m) = \sum_{l=0}^{L-1} x([\sigma_1 l + \tau_1]_{N_1}, [\sigma_2 l + \tau_2]_{N_2}) e^{-j\frac{2\pi}{L}ml}$$
$$= \sum_{l=0}^{L-1} \frac{1}{N} \sum_{\Omega} A_{(m_1,m_2)} e^{j2\pi\left[\frac{m_1[\sigma_1 l + \tau_1]}{N_1} + \frac{m_2[\sigma_2 l + \tau_2]}{N_2}\right]}$$
$$e^{-j\frac{2\pi}{L}ml}$$
$$= \frac{1}{N} \sum_{\Omega} A_{(m_1,m_2)} e^{j2\pi\left[\frac{m_1\tau_1}{N_1} + \frac{m_2\tau_2}{N_2}\right]}$$
$$\sum_{l=0}^{L-1} e^{j2\pi l\left[\frac{m_1\sigma_1}{N_1} + \frac{m_2\sigma_2}{N_2} - \frac{m}{L}\right]}$$
$$= \frac{L}{N} \sum_{\Omega} A_{(m_1,m_2)} e^{j2\pi\left[\frac{m_1\tau_1}{N_1} + \frac{m_2\tau_2}{N_2}\right]}$$
$$\delta\left[\frac{m_1\sigma_1}{N_1} + \frac{m_2\sigma_2}{N_2} - \frac{m}{L}\right] \quad (15)$$

where $N = N_1 N_2$, and $m = 0,1,\ldots,L-1$. And δ is the impulse function. This step is called bucketing. And the result of (15) is defined as a set of buckets. From (15), the following conclusions can be drawn:

Firstly, $Q_{\sigma_1,\sigma_2,\tau_1,\tau_2}(m)$ can be regarded as the projection of N/L points in the frequency matrix. If (μ_1', μ_2') is any pair of integers satisfying $\mu_1' \frac{L\sigma_1}{N_1} + \mu_2' \frac{L\sigma_2}{N_2} = 1$, those points (μ_1, μ_2) can be expressed as

$$\begin{cases} \mu_1 = [\mu_1' + c\sigma_2 L/N_2]_{N_1} \\ \mu_2 = [\mu_2' - c\sigma_1 L/N_1]_{N_2} \end{cases} \quad (16)$$

where c takes any integer.

Secondly, if the frequency value at the location (m_1, m_2) is $A_{(m_1,m_2)}$, it is projected to bucket (17) and the projected value is (18)

$$m = \left[\frac{L}{N_1} m_1 \sigma_1 + \frac{L}{N_2} m_2 \sigma_2\right]_L \quad (17)$$

$$Proj = \frac{L}{N} A_{(m_1,m_2)} e^{j2\pi\left[\frac{m_1\tau_1}{N_1} + \frac{m_2\tau_2}{N_2}\right]} \quad (18)$$

Finally, the location relationship of the three projections is the same, although the three DFTs are different.

Step 3: Define a set (19) to store large-value buckets. The non-zero frequencies of $x(s,t)$ will be estimated using the buckets.

$$\mathcal{J} = \{ m \in L || Q_{\sigma_1,\sigma_2,\tau_1,\tau_2}(m)|^2 > 0,$$
$$|Q_{\sigma_1,\sigma_2,\tau_1+1,\tau_2}(m)|^2 > 0,$$
$$|Q_{\sigma_1,\sigma_2,\tau_1,\tau_2+1}(m)|^2 > 0\} \quad (19)$$

In detail, for each bucket m belonging to (19), it is easy to derive 1-sparse if and only if the variance of $Q_{\sigma_1,\sigma_2,\tau_1,\tau_2}(m), Q_{\sigma_1,\sigma_2,\tau_1+1,\tau_2}(m), Q_{\sigma_1,\sigma_2,\tau_1,\tau_2+1}(m)$ equals zero. In other words, only one non-zero frequency is projected to bucket m. Suppose the location of this frequency is (m_1, m_2) and the amplitude is $A_{(m_1,m_2)}$. Therefore, the bucket values are (20) respectively.

$$Q_{\sigma_1,\sigma_2,\tau_1,\tau_2}(m) = \frac{L}{N} A_{(m_1,m_2)} e^{j2\pi\left[\frac{m_1\tau_1}{N_1} + \frac{m_2\tau_2}{N_2}\right]}$$

$$Q_{\sigma_1,\sigma_2,\tau_1+1,\tau_2}(m) = \frac{L}{N} A_{(m_1,m_2)} e^{j2\pi\left[\frac{m_1(\tau_1+1)}{N_1} + \frac{m_2\tau_2}{N_2}\right]}$$

$$Q_{\sigma_1,\sigma_2,\tau_1,\tau_2+1}(m) = \frac{L}{N} A_{(m_1,m_2)} e^{j2\pi\left[\frac{m_1\tau_1}{N_1} + \frac{m_2(\tau_2+1)}{N_2}\right]} \quad (20)$$

Then, the locations (m_1, m_2) of the nonzero frequency which is projected into bucket m are estimated to be (21), and the frequency value is estimated to be (22).

$$
\begin{cases}
m_1 = \left[\phi\left(\frac{Q_{\sigma_1,\sigma_2,\tau_1+1,\tau_2}(m)}{Q_{\sigma_1,\sigma_2,\tau_1,\tau_2}(m)}\right)\frac{N_1}{2\pi}\right]_{N_1} \\
m_2 = \left[\phi\left(\frac{Q_{\sigma_1,\sigma_2,\tau_1,\tau_2+1}(m)}{Q_{\sigma_1,\sigma_2,\tau_1,\tau_2}(m)}\right)\frac{N_2}{2\pi}\right]_{N_2}
\end{cases}
\tag{21}
$$

$$
A_{(m_1,m_2)} = \frac{N}{L}Q_{\sigma_1,\sigma_2,\tau_1,\tau_2}(m)e^{-j2\pi[\frac{m_1\tau_1}{N_1}+\frac{m_2\tau_2}{N_2}]}
\tag{22}
$$

where $\phi(a)$ denotes the phase of a. Therefore, most of the frequency components can be estimated from the buckets in $\mathcal{J}$. Define another set $\mathcal{A} = (m_1, m_2) \cup \mathcal{A}$ to store all the estimated frequencies.

Step 4: Perform iterations for T times, where T is an integer. The details are as follows. Firstly, execute Step 2 to bucketing. Secondly, remove the effect of estimated frequencies in $\mathcal{A}$ on bucket values:

$$
Q_{\sigma_1,\sigma_2,\tau_1,\tau_2}(m) = Q_{\sigma_1,\sigma_2,\tau_1,\tau_2}(m)
$$
$$
- \sum_{(m_1,m_2)\in\Sigma} \frac{L}{N}A_{(m_1,m_2)}e^{j2\pi[\frac{m_1\tau_1}{N_1}+\frac{m_2\tau_2}{N_2}]}
\tag{23}
$$

$$
\Sigma = \left\{(m_1,m_2) \in \mathcal{A} \Big| \frac{L}{N_1}m_1\sigma_1 + \frac{L}{N_2}m_2\sigma_2 = m\right\}
\tag{24}
$$

This can be achieved through Algorithm 2. Finally, execute Step 3 to estimate the remaining non-zero frequencies. If one location is estimated repeatedly, the estimated frequency values are added correspondingly.

Algorithm 2 Bucket algorithm.

Require: Modulated signals x, locations $\mathcal{A}$ and amplitudes X of the estimated frequencies, random parameters $\sigma_1, \sigma_2, \tau_1, \tau_2$.

Ensure: Buckets B subtracted the effect of the frequencies estimated previously.

1: $(N_1, N_2) = size(x)$
2: Initialize $hB = zeros(1, L), L = LCM(N_1, N_2)$
3: Extract $q_{\sigma_1,\sigma_2,\tau_1,\tau_2}(l)$ from x by (14), $l = 1 \to L$
4: $Q_{\sigma_1,\sigma_2,\tau_1,\tau_2} = FFT(q_{\sigma_1,\sigma_2,\tau_1,\tau_2}(l))$
5: **for** $(m_1, m_2) \in \mathcal{A}$ **do**
6:     get m by (17)
7:     $A_{(m_1,m_2)} = X(m_1, m_2)$
8:     get $Proj$ by (18)
9:     $hB(m) = hB(m) + Proj$
10: **end for**
11: $B = Q_{\sigma_1,\sigma_2,\tau_1,\tau_2} - hB$

Step 5: Multiply the estimation result (25) obtained from the above steps with another chirp function. And the 2D SFRFT result is finally given by (26).

$$
X(u, v) = \begin{cases} A_{(u,v)} & (u, v) \in \mathcal{A} \\ 0 & otherwise \end{cases}
\tag{25}
$$

$$
\hat{F}_{\alpha,\beta}(u, v) = \sqrt{\frac{(\sin\alpha - j\cos\alpha)(\sin\beta - j\cos\beta)}{M_1 M_2}}X(u, v)e^{j\frac{u^2\Delta u^2}{2\tan\alpha}+j\frac{v^2\Delta v^2}{2\tan\beta}}
\tag{26}
$$

where $u = 0, 1, \ldots, N_1 - 1$ and $v = 0, 1, \ldots, N_2 - 1$. $\Delta u, \Delta v$ are the sampling interval of the two dimensions in the fractional Fourier domain. α, β are real numbers representing fractional orders of the two dimensions.

Remark 1. The algorithm idea and flow are similar to the above steps for $\sin\alpha < 0, \sin\beta < 0$ situations. And the main differences are as follows: In Step2, perform an IFFT on the extracted random slices and multiply by N. In Step3, estimate that the frequency projecting into 1-sparse bucket m has location (27) and the amplitude is (28).

$$
\begin{cases}
m_1 = \left[-\phi\left(\frac{Q_{\sigma_1,\sigma_2,\tau_1+1,\tau_2}(m)}{Q_{\sigma_1,\sigma_2,\tau_1,\tau_2}(m)}\right)\frac{N_1}{2\pi}\right]_{N_1} \\
m_2 = \left[-\phi\left(\frac{Q_{\sigma_1,\sigma_2,\tau_1,\tau_2+1}(m)}{Q_{\sigma_1,\sigma_2,\tau_1,\tau_2}(m)}\right)\frac{N_2}{2\pi}\right]_{N_2}
\end{cases}
\tag{27}
$$

$$
A_{(m_1,m_2)} = Q_{\sigma_1,\sigma_2,\tau_1,\tau_2}(m)e^{j2\pi[\frac{m_1\tau_1}{N_1}+\frac{m_2\tau_2}{N_2}]}
\tag{28}
$$

In Step4, Eq. (23) is replaced by (29). These are easy to derive.

$$
Q_{\sigma_1,\sigma_2,\tau_1,\tau_2}(m) = Q_{\sigma_1,\sigma_2,\tau_1,\tau_2}(m) - \sum_{(m_1,m_2)\in\Sigma} A_{(m_1,m_2)}e^{j2\pi[\frac{m_1\tau_1}{N_1}+\frac{m_2\tau_2}{N_2}]}
\tag{29}
$$

4. Robust 2D SFRFT algorithm

This section will present the robust two-dimensional sparse fractional Fourier transform (robust 2D SFRFT) algorithm for noisy signals. In signal processing, complex Gaussian noises are common. In communication theory, narrow-band white Gaussian noises can be represented by a cyclic symmetric complex Gaussian process when represented by an equivalent low-pass representation. Assume that the sparse signal $f(s, t)$ with size (N_1, N_2) is polluted by additive noise which obeys a cyclic symmetric complex Gaussian distribution $r_f(s, t) \sim CN(0, \eta^2)$. Therefore, the fractional Fourier domain of the signal is approximated sparse. It consists of several important frequencies and negligible noises. Our algorithm will estimate its best approximation, that is, all significant frequencies. The noises affect the bucket values, and step 3 of the proposed 2D SFRFT algorithm needs to be improved.

4.1. Effect of noises on buckets

When the original signal $f(s, t)$ is interspersed with noises $r_f(s, t) \sim CN(0, \eta^2)$, $x(s, t)$ is also polluted by additive noises $r_x(s, t) \sim CN(0, \eta^2)$ after Step1. Correspondingly, the Fourier domain contains noises $r_X(u, v) \sim CN(0, \eta_f^2)$ where $\eta_f^2 = N\eta^2, N = N_1 N_2$. Therefore, the buckets are changed to (30),

$$
\hat{Q}_{\sigma_1,\sigma_2,\tau_1,\tau_2}(m) = \frac{L}{N}\sum_{\Omega\cap\Upsilon_1} A_{(m_1,m_2)}e^{j2\pi[\frac{m_1\tau_1}{N_1}+\frac{m_2\tau_2}{N_2}]}
$$
$$
+ \frac{L}{N}\sum_{\Upsilon_1} r_X(u, v)e^{j2\pi[\frac{u\tau_1}{N_1}+\frac{v\tau_2}{N_2}]}
\tag{30}
$$

where the meaning of the parameters is the same as that in Section 3 and

$$
\Upsilon_1 = \left\{(u, v)\Big|\left[\frac{Lu\sigma_1}{N_1}+\frac{Lv\sigma_2}{N_2}\right]_L = m\right\}
\tag{31}
$$

Meanwhile, $u = 0, 1, \ldots N_1 - 1$ and $v = 0, 1, \ldots N_2 - 1$.

It is clear from (30) that most of the buckets' values are no longer equal to zero, while values of buckets with significant frequencies still are larger than that of noise-only buckets. Therefore, The set $\hat{\mathcal{J}}$ of large buckets needs to be estimated by increasing a threshold ε:

$$
\hat{\mathcal{J}} = \{m \in L||\hat{Q}_{\sigma_1,\sigma_2,\tau_1,\tau_2}(m)|^2 > \varepsilon,
$$
$$
|\hat{Q}_{\sigma_1,\sigma_2,\tau_1+1,\tau_2}(m)|^2 > \varepsilon,
$$
$$
|\hat{Q}_{\sigma_1,\sigma_2,\tau_1,\tau_2+1}(m)|^2 > \varepsilon\}
\tag{32}
$$

We can choose $\varepsilon = -2L\eta^2 \ln P_{fa}$, where P_{fa} is the false alarm probability of large-value buckets detection. The specific analysis is as follows.

Assume that bucket m^0 contains no significant frequencies, and bucket m^1 contains one significant frequency with minimum amplitude $A_{(m_1, m_2)}$. According to (30), the bucket values obey complex Gaussian distribution:

$$\hat{Q}_{\sigma_1, \sigma_2, \tau_1, \tau_2}(m^0) \sim CN(0, \eta_0^2) \tag{33}$$

$$\hat{Q}_{\sigma_1, \sigma_2, \tau_1, \tau_2}(m^1) \sim \frac{L}{N} A_{(m_1, m_2)} e^{j2\pi[\frac{m_1\tau_1}{N_1} + \frac{m_2\tau_2}{N_2}]} + CN(0, \eta_0^2) \tag{34}$$

where $\eta_0^2 = L\eta^2$. Based on [57], let $\theta(m) = \left|\hat{Q}_{\sigma_1, \sigma_2, \tau_1, \tau_2}(m)\right|^2$, then $\theta(m)$ follow the chi-square distribution with the probability density function

$$f(\theta(m^0)) = \frac{1}{2} e^{-\frac{\theta(m^0)}{2\eta_0^2}} \tag{35}$$

$$f(\theta(m^1)) = \frac{1}{2\sqrt{\eta_0^2 \pi}} (a\theta(m^1))^{-\frac{1}{4}} e^{-\frac{(\sqrt{\theta(m^1)} - \sqrt{a})^2}{\eta_0^2}} \tag{36}$$

where $a = \frac{L}{N} A_{(m_1, m_2)}$. Therefore, the probability of $\theta(m^0) > \varepsilon$ is

$$P_{fa} = e^{-\frac{\varepsilon}{2L\eta^2}} \tag{37}$$

And (37) indicates the probability of a non-large value bucket being detected as a large value bucket, i.e., the probability of a false alarm. It is easy to deduce that the large-value bucket threshold $\varepsilon = -2L\eta^2 \ln P_{fa}$. Meanwhile, the probability of $\theta(m^1) > \varepsilon$ is

$$P_d = \frac{\eta}{2} \sqrt{\frac{L}{\pi}} (a\varepsilon)^{-\frac{1}{4}} e^{-\frac{(\sqrt{\varepsilon} - \sqrt{a})^2}{L\eta^2}} \tag{38}$$

And the probability of a large value bucket being detected correctly is not less than P_d.

Moreover, the bucket m is 1-sparse when the variance of $\hat{Q}_{\sigma_1, \sigma_2, \tau_1, \tau_2}(m)$, $\hat{Q}_{\sigma_1, \sigma_2, \tau_1+1, \tau_2}(m)$, $\hat{Q}_{\sigma_1, \sigma_2, \tau_1, \tau_2+1}(m)$ is greater than a threshold δ. It is known empirically that δ is a small positive number.

4.2. Effect of noises on positions

Due to the noises, there are errors in the frequency location estimated by (23). Suppose the bucket m is 1-sparse. The location and the amplitude of the significant frequency projected to bucket $m \in \hat{\mathcal{J}}$ are (m_1, m_2) and $A_{(m_1, m_2)}$, respectively. For m_1, the result of the phase function is (39).

As a result, the phase error ϕ_1^{err} at row position m_1 can be expressed as (40).

$$\phi_1^{err} = \phi\left(\frac{A_{(m_1, m_2)} e^{j2\pi[\frac{m_1\tau_1}{N_1} + \frac{m_2\tau_2}{N_2}]} + \sum_{\Upsilon_1} r_X(u,v) e^{j2\pi[\frac{u\tau_1 + u - m_1}{N_1} + \frac{v\tau_2}{N_2}]}}{A_{(m_1, m_2)} e^{j2\pi[\frac{m_1\tau_1}{N_1} + \frac{m_2\tau_2}{N_2}]} + \sum_{\Upsilon_1} r_X(u,v) e^{j2\pi[\frac{u\tau_1}{N_1} + \frac{v\tau_2}{N_2}]}} \right) \tag{40}$$

Then the error of the row position estimation is equal to

$$m_1^{err} = \left[round(\phi_1^{err} \frac{N_1}{2\pi}) \right]_{N1} \tag{41}$$

where $round()$ is a rounding function. It is worth noting that (41) is a random variable since $r_X(u, v)$ are random variables. If existing an integer γ_1 that satisfies $\left| m_1^{err} \right| \leq \gamma_1$ with high probability, the m_1 is a value in the set Λ_1:

$$\Lambda_1 = \left\{ \hat{m}_1 - \gamma_1, \ldots, \hat{m}_1, \hat{m}_1 + 1, \ldots, \hat{m}_1 + \gamma_1 \right\}_{N_1} \tag{42}$$

where $\hat{m}_1$ is the row location estimated by (21), and $\{\}_{N_1}$ denotes that all elements in Λ_1 are modulo N_1.

Similarly, if column position $\hat{m}_2$ is estimated by (21), the error of the column position estimation is equal to

$$m_2^{err} = \left[round(\phi_2^{err}) \frac{N_2}{2\pi} \right]_{N2} \tag{43}$$

where ϕ_2^{err} is the phase error of the column m_2, as expressed in (44).

$$\phi_2^{err} = \phi\left(\frac{A_{(m_1, m_2)} e^{j2\pi[\frac{m_1\tau_1}{N_1} + \frac{m_2\tau_2}{N_2}]} + \sum_{\Upsilon_1} r_X(u,v) e^{j2\pi[\frac{u\tau_1}{N_1} + \frac{v\tau_2 + v - m_2}{N_2}]}}{A_{(m_1, m_2)} e^{j2\pi[\frac{m_1\tau_1}{N_1} + \frac{m_2\tau_2}{N_2}]} + \sum_{\Upsilon_1} r_X(u,v) e^{j2\pi[\frac{u\tau_1}{N_1} + \frac{v\tau_2}{N_2}]}} \right) \tag{44}$$

If existing an integer γ_2 that satisfies $\left| m_2^{err} \right| \leq \gamma_2$ with high probability, the column position m_2 is a value in the set Λ_2,

$$\Lambda_2 = \left\{ \hat{m}_2 - \gamma_2, \ldots, \hat{m}_2, \hat{m}_2 + 1, \ldots, \hat{m}_2 + \gamma_2 \right\}_{N_2} \tag{45}$$

4.3. The robust positions estimation algorithm

Based on the above analysis, we will find suitable γ_1, γ_2 and estimate the correct positions in the sets Λ_1 and Λ_2.

4.3.1. Estimation of position error thresholds

Assume that the probability that the true row position m_1 is contained in the set Λ_1 is at least P_1^γ. Then, the row position error threshold γ_1 must satisfy the following equation:

$$P(|m_1^{err}| \leq \gamma_1) = P\left(|\phi_1^{err}| \leq (\gamma_1 + 0.5) \frac{2\pi}{N_1} \right) \geq P_1^\gamma \tag{46}$$

The expression for ϕ_1^{err} is complex, and we estimate its probability

$$\phi\left(\frac{\hat{Q}_{\sigma_1, \sigma_2, \tau_1+1, \tau_2}(m)}{\hat{Q}_{\sigma_1, \sigma_2, \tau_1, \tau_2}(m)} \right) = \phi\left(\frac{\frac{L}{N} A_{(m_1, m_2)} e^{j2\pi[\frac{m_1\tau_1 + m_1}{N_1} + \frac{m_2\tau_2}{N_2}]} + \frac{L}{N} \sum_{\Upsilon_1} r_X(u,v) e^{j2\pi[\frac{u\tau_1 + u}{N_1} + \frac{v\tau_2}{N_2}]}}{\frac{L}{N} A_{(m_1, m_2)} e^{j2\pi[\frac{m_1\tau_1}{N_1} + \frac{m_2\tau_2}{N_2}]} + \frac{L}{N} \sum_{\Upsilon_1} r_X(u,v) e^{j2\pi[\frac{u\tau_1}{N_1} + \frac{v\tau_2}{N_2}]}} \right)$$

$$= \phi\left(\frac{e^{j2\pi\frac{m_1}{N_1}} [A_{(m_1, m_2)} e^{j2\pi[\frac{m_1\tau_1}{N_1} + \frac{m_2\tau_2}{N_2}]} + \sum_{\Upsilon_1} r_X(u,v) e^{j2\pi[\frac{u\tau_1 + u - m_1}{N_1} + \frac{v\tau_2}{N_2}]}]}{A_{(m_1, m_2)} e^{j2\pi[\frac{m_1\tau_1}{N_1} + \frac{m_2\tau_2}{N_2}]} + \sum_{\Upsilon_1} r_X(u,v) e^{j2\pi[\frac{u\tau_1}{N_1} + \frac{v\tau_2}{N_2}]}} \right)$$

$$= 2\pi\frac{m_1}{N_1} + \phi\left(\frac{A_{(m_1, m_2)} e^{j2\pi[\frac{m_1\tau_1}{N_1} + \frac{m_2\tau_2}{N_2}]} + \sum_{\Upsilon_1} r_X(u,v) e^{j2\pi[\frac{u\tau_1 + u - m_1}{N_1} + \frac{v\tau_2}{N_2}]}}{A_{(m_1, m_2)} e^{j2\pi[\frac{m_1\tau_1}{N_1} + \frac{m_2\tau_2}{N_2}]} + \sum_{\Upsilon_1} r_X(u,v) e^{j2\pi[\frac{u\tau_1}{N_1} + \frac{v\tau_2}{N_2}]}} \right) \tag{39}$$

density function by the Parzen window method. Subsequently, we estimate the probability of $P(|m_1^{err}| \leq \tilde{\gamma}_1)$ for integer $\tilde{\gamma}_1$ which increments from 0. And the smallest $\tilde{\gamma}_1$ satisfying (46) is found to be γ_1. Similarly, we can estimate the threshold γ_2 of column position error.

4.3.2. Estimation of positions

For the 1-sparse bucket $m \in \hat{\mathcal{J}}$, the row position m_1 belongs to Λ_1 with a probability no less than P_1^γ. And the column position m_2 belongs to Λ_2 with a probability no less than P_2^γ. Thus, we can obtain a set Υ_2 of possible positions for significant frequencies, where

$$\Upsilon_2 = \{(u,v)|u \in \Lambda_1, v \in \Lambda_2\} \tag{47}$$

In addition, according to the mapping of the bucketing, the significant frequencies must be contained in the set Υ_1

$$\Upsilon_1 = \left\{ (u,v) \,\middle|\, \left[\frac{Lu\sigma_1}{N_1} + \frac{Lv\sigma_2}{N_2} \right]_L = m \right\} \tag{48}$$

In summary, the set of possible locations can be reduced to

$$\Pi^0 = \Upsilon_1 \cap \Upsilon_2 \tag{49}$$

If Π^0 contains only one element, the location (m_1, m_2) is estimated successfully. Otherwise, we will execute inner loops to reduce the set Π^0. Specific details are as Algorithm 3 and follow.

Algorithm 3 Innerloop algorithm.

Require: Modulated signals x, locations $\mathcal{A}$ and amplitudes X of the estimated frequencies previously, the set Π^0 of possible locations for a significant frequency.
Ensure: Updated $\mathcal{A}, X$.
1: **for** $s = 1 \rightarrow N_{in}$ **do**
2:     Choose τ_1' from $0 \rightarrow N_1 - 1$ randomly
3:     Choose τ_2' from $0 \rightarrow N_2 - 1$ randomly
4:     $D = ones(1, length(\Pi^{s-1}))$
5:     **while** D contains repeated indices **do**
6:         $\sigma_1', \sigma_2' \leftarrow Get(N_1, N_2)$
7:         Π^{s-1} bucketed into D by (17)
8:     **end while**
9:     $B' \leftarrow Bucket(x, \mathcal{A}, X, \sigma_1', \sigma_2', \tau_1', \tau_2')$
10:     $\mathcal{L} = \{m \,||B'(m)|^2 > \varepsilon\}$
11:     $\Pi^s = D^{-1}(D \cap \mathcal{L})$
12:     **if** $|\Pi^s| = 1$ **then**
13:         $\mathcal{A} = \mathcal{A} \cup \Pi^s$
14:         $X(\Pi^s) += \frac{N}{L} B(1, j) e^{-j2\pi \Pi^s [\frac{\tau_1}{N_1} : \frac{\tau_2}{N_2}]}$
15:         Break
16:     **end if**
17: **end for**

After the $(s-1)$th inner loop, suppose Π^0 is reduced to Π^{s-1} which has more than one element. During the sth inner loop, we determine the new random slice parameters $\sigma_1^s, \sigma_2^s, \tau_1^s, \tau_2^s$, which guarantee that all elements in Π^{s-1} are divided into different buckets. By bucketing with $\sigma_1^s, \sigma_2^s, \tau_1^s, \tau_2^s$ and subtracting the effect of the previous iterations, the new large-value buckets are obtained. Because the significant frequencies must be in the large value buckets, elements that are not assigned to new large-value buckets can be excluded from Π^{s-1}. And the set of possible locations is updated to Π^s. If Π^s contains only one element, the location (m_1, m_2) is estimated successfully.

Generally, the position (m_1, m_2) can be estimated by executing only a few inner loops. To prevent infinite iterations caused by the wrong Υ_2, we set the maximum number N_{in} of inner loops. If the termination condition is not reached after N_{in}th inner loop, stop the inner loops and output an empty position set.

4.3.3. Robust 2D SFRFT algorithm flow

Based on the estimation of position error thresholds and positions, the robust 2D SFRFT algorithm is proposed. And the pseudocode is shown in Algorithm 4. If the large-value bucket detection threshold ε, 1-sparse bucket detection threshold δ, and the position error thresholds γ_1, γ_2 are equal to zero, the robust 2D SFRFT algorithm in Algorithm 4 is simplified to the 2D SFRFT algorithm proposed in Section 3.

Algorithm 4 Robust 2D SFRFT algorithm.

Require: The original signal $f(s,t)$ with size (N_1, N_2), fractional orders (α, β), sampling interval $(\Delta s, \Delta t)$, position error thresholds (γ_1, γ_2), False alarm probability P_{fa} of large-value buckets detection.
Ensure: Fractional Fourier domain spectrum $\hat{F}_{\alpha,\beta}(u,v)$.
1: Initialize the position and amplitude of the frequencies estimated previously $\mathcal{A} = [\,], X = zeros(N_1, N_2)$;
2: Moderate $f(s,t)$ by (12) to get $x(s,t)$
3: **for** $i = 1 \rightarrow T$ **do**
4:     Choose τ_1 from $0 \rightarrow N_1 - 1$ randomly
5:     Choose τ_2 from $0 \rightarrow N_2 - 1$ randomly
6:     $\sigma_1, \sigma_2 \leftarrow Get(N_1, N_2)$
7:     $B_0 \leftarrow Bucket(x, \mathcal{A}, X, \sigma_1, \sigma_2, \tau_1, \tau_2)$
8:     $B_1 \leftarrow Bucket(x, \mathcal{A}, X, \sigma_1, \sigma_2, \tau_1 + 1, \tau_2)$
9:     $B_2 \leftarrow Bucket(x, \mathcal{A}, X, \sigma_1, \sigma_2, \tau_1, \tau_2 + 1)$
10:     Find the set $\hat{\mathcal{J}}$ by (32)
11:     $B = [B_0(\hat{\mathcal{J}}); B_1(\hat{\mathcal{J}}); B_2(\hat{\mathcal{J}})]$
12:     **for** $j = 1 \rightarrow length(\hat{\mathcal{J}})$ **do**
13:         **if** $var(abs(B(:,j))) < \delta$ **then**
14:             $m = \hat{\mathcal{J}}(j)$
15:             $\hat{m}_1 = \left[\phi\left(\frac{B(2,j)}{B(1,j)} \right) \frac{N_1}{2\pi} \right]_{N_1}$
16:             $\hat{m}_2 = \left[\phi\left(\frac{B(3,j)}{B(1,j)} \right) \frac{N_2}{2\pi} \right]_{N_2}$
17:             Find the set Π^0 by (49)
18:             **if** $|\Pi^0| = 1$ **then**
19:                 $\mathcal{A} = \mathcal{A} \cup \Pi^0$
20:                 $X(\Pi^0) += \frac{N}{L} B(1,j) e^{-j2\pi \Pi^0 [\frac{\tau_1}{N_1} : \frac{\tau_2}{N_2}]}$
21:             **else**
22:                 $\mathcal{A}, X \leftarrow Innerloop(x, \mathcal{A}, X, \Pi^0)$
23:             **end if**
24:         **end if**
25:     **end for**
26: **end for**
27: Moderate $X(u,v)$ by (26) to get $\hat{F}_{\alpha,\beta}(u,v)$

---

5. Simulations

In this section, to verify the advantages of the 2D SFRFT algorithm, the efficiency and L_2 error will be compared with the conventional methods. Then, the position error threshold in the robust 2D SFRFT algorithm will be analyzed. Subsequently, the convergence of the robust 2D SFRFT algorithm will be analyzed, specifically in terms of the number of iterations, the number of inner loops, and the probability of strict estimation. Finally, the sample complexity, the runtime complexity, and the estimated probability of one significant frequency will be given.

5.1. Efficiency and L_2 error of the 2D SFRFT

In this subsection, we will simulate the proposed 2D SFRFT algorithm and compare the efficiency and L_2 error with the conventional method. Traditionally, the 2D DFRFT of signals $f(s,t)$ with
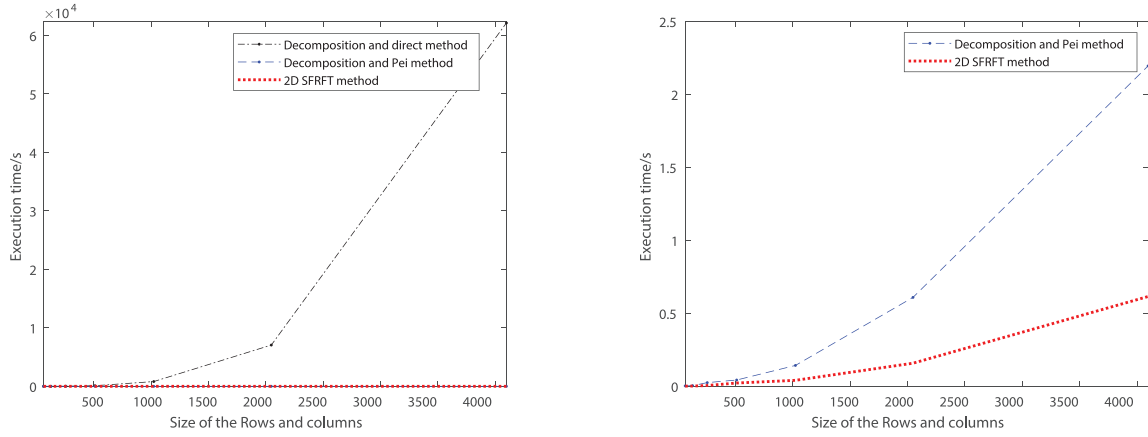
(a) Comparison between decomposition and direct method, decomposition and Pei method, 2D SFRFT method.

(b) Comparison between decomposition and Pei method, 2D SFRFT method.

Fig. 1. Comparison of running times.

order (α, β) is obtained by decomposing into 1D DFRFT. Specifically, all the row vectors of $f(s, t)$ are performed the 1D DFRFT with fractional order α respectively, and a new 2D signal $\hat{f}(s, t)$ is formed according to the original position. Then, all the column vectors of $\hat{f}(s, t)$ are performed the 1D DFRFT with fractional order β respectively, and the 2D DFRFT $\hat{F}_{\alpha, \beta}(u, v)$ is obtained according to the original position. The fast 2D DFRFT algorithms can be obtained utilizing the fast accomplish of 1D DFRFT. As described in Section 2.1, the Pei-type 1D DFRFT can be decomposed into two times of multiplication with chirp signals and one FFT operation to quickly achieve. We simulate the decomposition and direct method, decomposition and Pei method, and 2D SFRFT method.

The experimental signals with size $N_1 = N_2 \in \{2^6, 2^7, 2^8, 2^9, 2^{10}, 2^{11}, 2^{12}\}$ are noise-free. And its fractional Fourier the spectrum contains five non-zero frequencies with random amplitudes and random positions. The comparison of runtime between decomposition and direct method, decomposition and Pei method, 2D SFRFT method is shown in Fig. 1a. It is clear that the direct method is time expensive as the signal sizes increase. The running time of Pei's fast computational method and the 2D SFRFT method are clustered in a small range amplified in Fig. 1b. Fixing the signal sizes, the runtime of 2D SFRFT is smaller than that of the decomposition and Pei method. And the runtime of 2D SFRFT grows more slowly with signal sizes. It shows that our method is more efficient. The comparison of L_2 error between the Pei method and the 2D SFRFT method is displayed in Fig. 2. The L_2 errors of the 2D SFRFT method are clustered at 10^{-12}, while the errors of the decomposition and Pei method are 4.5×10^{-9} on average. In summary, 2D SFRFT is excellent in both efficiency and accuracy.

5.2. Analysis of position error thresholds

In this subsection, we will discuss the relationship between the error thresholds and the signal sizes, SNR, and location probability. Without loss of generality, the simulations address the estimation of row positions in this subsection. One might set the fractional Fourier transform spectrum of the signals $f(s, t)$ to contain one significant frequency whose locations (m_1, m_2) are random. And assuming that the time domain signals $f(s, t)$ with size (N_1, N_2) are polluted by additive noise which obeys a cyclic symmetric complex Gaussian distribution $r_f(s, t) \sim CN(0, 1)$. The amplitude of the signals can be determined by

the SNR. Random parameters $\sigma_1, \sigma_2, \tau_1, \tau_2$ are used to perform the bucketing operation. For the 1-sparse bucket $m \in \hat{\mathcal{J}}$, the row position m_1 belongs to Λ_1 with a probability no less than P_1^γ.

Based on the subsection of *Estimation of position error thresholds*, the threshold γ_1 of the row position error m_1^{err} can be determined based on row location probability P_1^γ and the probability density function of the phase error ϕ_1^{err}. It is easy to know from (40) that the phase error ϕ_1^{err} is influenced by (m_1, m_2), Υ_1 and SNR.

First, by the Parzen window method, we estimate the probability density function with different random significant frequency locations (m_1, m_2) as shown in Fig. 3. Where, $N1 = N2 = 256$ and SNR = 11.8351 dB. Fig. 3 indicates that the probability density of the phase error ϕ_1^{err} is similar to the Gaussian distribution. The phase errors ϕ_1^{err} are concentrated at zero and have almost the same distribution for different (m_1, m_2). If the row position probability P_1^γ is set to 0.999, it can be derived that the position error threshold γ_1 is equal to 2.

Moreover, the relationship between SNR, row position probability P_1^γ, and row position error threshold γ_1 is explored. We discuss the values of γ_1 when the row position probability P_1^γ is equal to 0.95, 0.98, 0.99, 0.999, 0.9999. The 1-sparse random signals of size (256, 256) are simulated and we consider SNR of 11.8351 dB, 1.8384 dB, −3.1534 dB, and −8.1777 dB. The result is shown in Fig. 4. If there is no noise, the threshold value takes the value of 0 and 2D SFRFT proposed in Section 3 is chosen. And noise increase leads to an increase in the position error threshold γ_1 if the position probability P_1^γ is fixed. Consistent with common sense, the threshold γ_1 increases with the predetermined position probability P_1^γ. The probability density of the phase error ϕ_1^{err} is clustered around zero and has a small value on the boundary. Therefore, the position error threshold γ_1 grows slowly when the position probability P_1^γ is small, while it increases exponentially when P_1^γ is greater than 0.999.

Finally, the relationship between signal sizes (N_1, N_2) and row position error threshold γ_1 is explored. From (48), it can be seen that Υ_1 is determined by the signal sizes (N_1, N_2) and σ_1, σ_2, m. In the robust 2D SFRFT algorithm, σ_1, σ_2 take random values and the large-value bucket m is also random. Therefore, only the effect of the signal sizes (N_1, N_2) on the row position error threshold γ_1 is considered. Assume that the SNR of all simulated signals is about 11.7719 dB. And the position probability P_1^γ is equal to 0.9999, which is a high-performance state. The row position
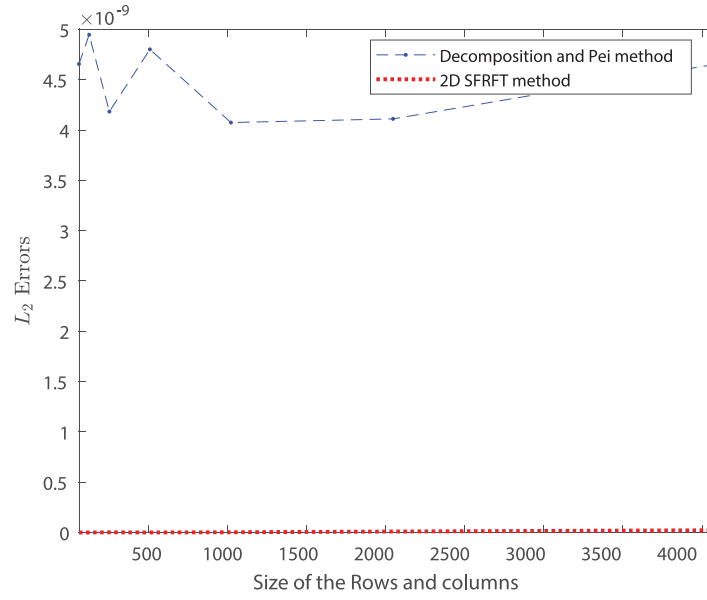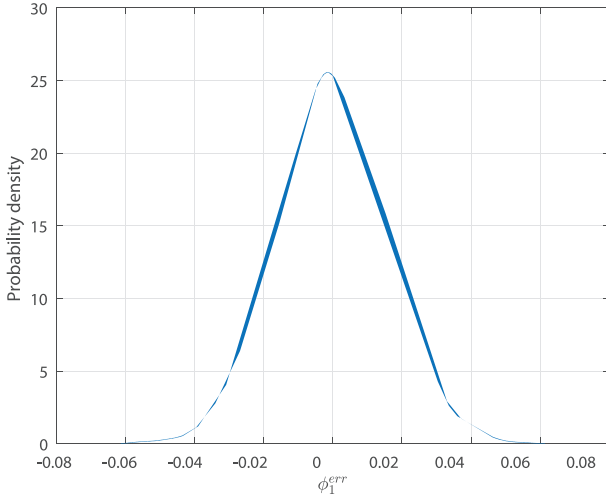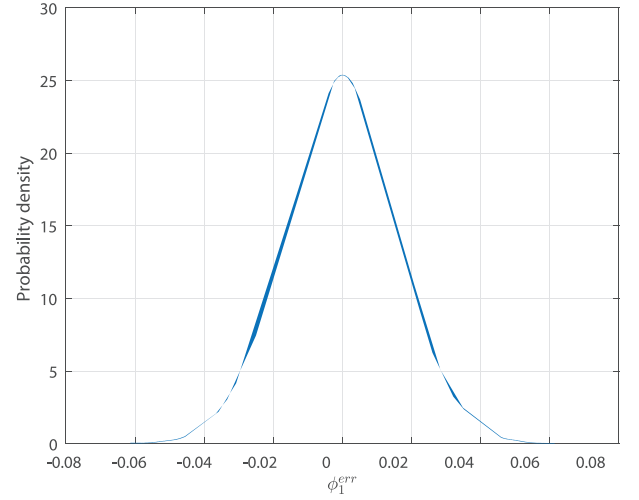
Fig. 2. Comparison of L_2 error between decomposition and Pei method, 2D SFRFT method.

(a) $(m_1, m_2) = (76, 75)$.

(b) $(m_1, m_2) = (244, 37)$.

Fig. 3. Probability density of phase error ϕ_1^{err} with different random significant frequency locations (m_1, m_2).

Table 1
Row position error threshold γ_1 with different signal sizes (N_1, N_2).

$N_2 \setminus N_1$	2^6	2^7	2^8	2^9	2^{10}	2^{11}	2^{12}
2^6	1	2	2	1	1	1	1
2^7	1	2	2	1	1	1	0
2^8	1	1	3	3	2	2	1
2^9	0	1	2	4	5	4	3
2^{10}	0	1	1	3	5	7	6
2^{11}	0	0	1	2	4	8	10
2^{12}	0	0	1	1	3	6	11

errors thresholds for different signal sizes are shown in Table 1. It can be seen that the row position error threshold γ_1 is much smaller than the signal sizes. For a fixed N_1, the row location error threshold γ_1 is maximum if $N_2 = N_1$. For convenience, we can select the value of γ_1 from Table 1 directly. Correspondingly, we can select the value of γ_2 from Table 1 by swapping N_1 and N_2.

5.3. Convergence of the robust 2D SFRFT algorithm

In this subsection, we will discuss the effect of SNR and signal sparsity k on the convergence of the algorithm. Specifically, we will discuss the number of iterations, the number of inner loops, and the probability of correct estimation of the robust 2D SFRFT algorithm.

The experimental signals $f(s, t)$ with size (2048,2048) are k-sparse in the fractional Fourier domain, where $k \in [10, 20, 30, 40, 50, 60, 80, 100]$. The locations of the k-significant frequencies are chosen randomly. It is assumed that the amplitudes of the significant frequencies are equal. The signals $f(s, t)$ are polluted by additive noise which obeys a cyclic symmetric complex Gaussian distribution $r_f(s, t) \sim CN(0, 1)$. The SNR of the time domain signals $f(s, t)$ are set to 17.7707 dB, 7.7738 dB, and -3.229 dB. And the values of 1-sparse buckets detection thresholds δ and false alarm probability P_{fa} of large-value buckets detection are shown in Table 2. The threshold ε for large-value buckets detection is determined by $\varepsilon = -2L \ln P_{fa}$. Let the position
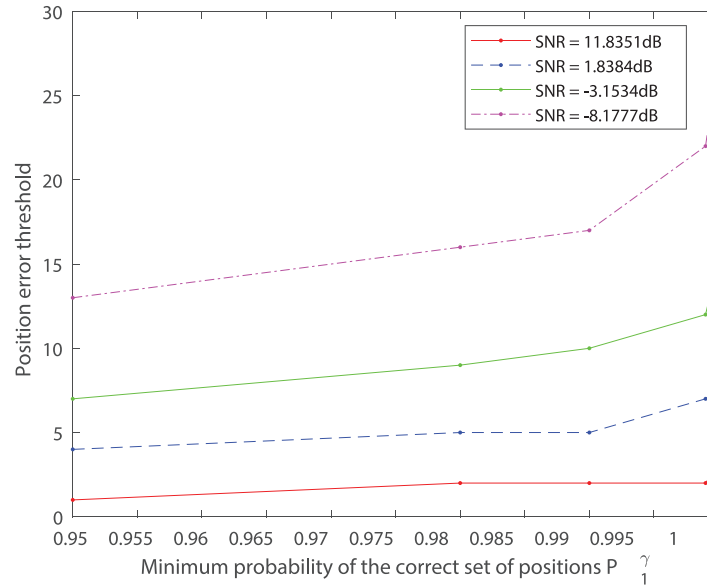
Fig. 4. Row position error threshold γ_1 with different SNR and row location probability P_1^γ.

Table 2
Threshold parameters at different SNR.

SNR(dB)	P_{fa}	ε
17.7707	0.1	10,000
7.7738	0.002	10,000
−3.229	0.05	2000

Table 3
Number of iterations for different signals.

SNR(dB)\k	10	20	30	40	50	60	80	100
17.7707	1	2	2	2	2	2	2	2
7.7738	1	2	2	2	2	2	2	2
-3.229	2	3	3	3	4	4	4	5

probability P_1^γ, P_2^γ be equal to 0.999, then the row position error threshold γ_1 and the column position error threshold γ_2 are pre-calculated through the Parzen window. Monte Carlo experiments are done using the above parameters to perform a robust 2D SFRFT algorithm on the signals.

First, the minimum number of iterations required by the robust 2D SFRFT algorithm is shown in Table 3. On the one hand, the number of iterations grows with the decrease of SNR, because the likelihood of important frequencies being estimated is reduced. On the other hand, the increase in sparsity aggravates the task of the algorithm, and therefore the number of iterations increases. In conclusion, the robust 2D SFRFT algorithm is convergent and several iterations are required to complete the estimation of the fractional Fourier spectrum.

Second, the average number of inner loops for estimating the location of each significant frequency is shown in Fig. 5. From the previous subsection, it is clear that the location error thresholds are smaller for high SNR. This means that the set of possible locations Π^0 has a smaller capacity. Therefore, the robust 2D SFRFT algorithm can end up the inner loop faster. Fig. 5 also demonstrates that signals with high SNR require fewer numbers of inner loops. In addition, it can be seen from Fig. 5 that the number of inner loops increases when the number of significant frequencies increases. This is because there are more large-value buckets in the re-bucketing of the inner loop. And the probability of non-significant frequencies being divided into large-value buckets in-

creases. The set Π^0 of possible locations is reduced more slowly. Therefore, more inner loops are needed to estimate the position.

Finally, Fig. 6 shows the probability that the estimated locations of all significant frequencies match the true locations exactly. It is not difficult to obtain that the robust 2D SFRFT algorithm performs better when applied to signals with higher SNR and more sparse. For SNR = 17.7707 dB, the probability of correct estimation is not less than 97%, regardless of the sparsity. When $k < 60$, the probability of accurate estimation is at least 94%, regardless of the SNR. However, if SNR = −3.229 dB and $k = 100$, the robust 2D SFRFT algorithm cannot estimate the fractional Fourier spectrum perfectly, and an example is shown in Fig. 7. Where the red circles indicate the true locations and the blue '×' indicate the locations estimated by the robust 2D SFRFT algorithm. There are a few unestimated significant frequencies and there are a few locations that are estimated as significant frequencies incorrectly. It is worth noting that most of the significant frequencies of the original signal are correctly estimated.

5.4. Complexity and probability analysis

5.4.1. Sample complexity

For the case of no noise, the iteration of 2D SFRFT performs FFT only for slices. Therefore, only the corresponding sample points are needed to multiply the Chirp signal in Step 1. Suppose the signal sizes are (N_1, N_2). A slice contains $L = LCM(N_1, N_2)$ samples, and three slices are needed for each iteration. If the number of iterations is T, then at most $3LT$ samples are used. Therefore, the sample complexity of 2D SFRFT is $O(LT)$.

For the case of noise, assume that the sparsity of the signals is k and the average number of inner loops is s to estimate per significant frequency. Then, the total number of inner loops is about sk. Since one slice with size L is extracted in each inner loop, the sample complexity of the robust 2D SFRFT is $O(L(T + sk))$.

5.4.2. Runtime complexity

For the case of no noise, Step1 takes $3LT$ times complex multiplications and Step5 takes k times complex multiplications. The remaining steps are iterative processes, which mainly contain the DFT of slices and the evaluation of the L buckets. The DFT is performed by FFT with the runtime complexity $O(LlogL)$. And the running time complexity of the T iterative processes is
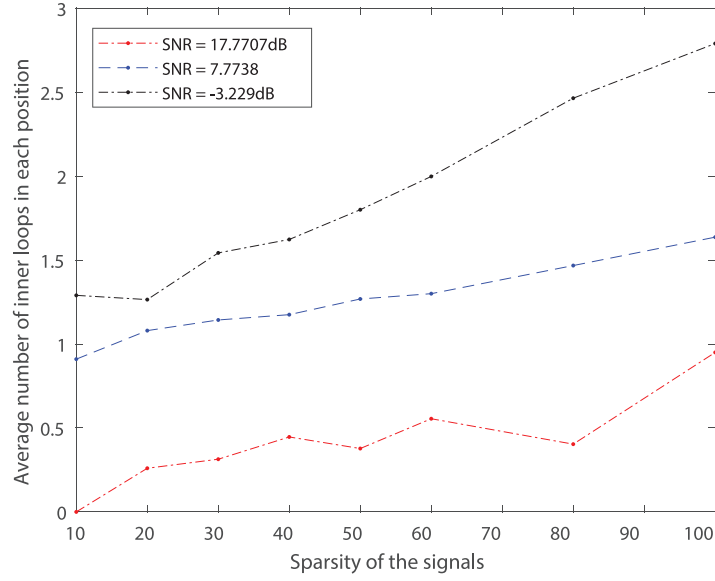
Fig. 5. The average number of inner loops for each significant frequency.
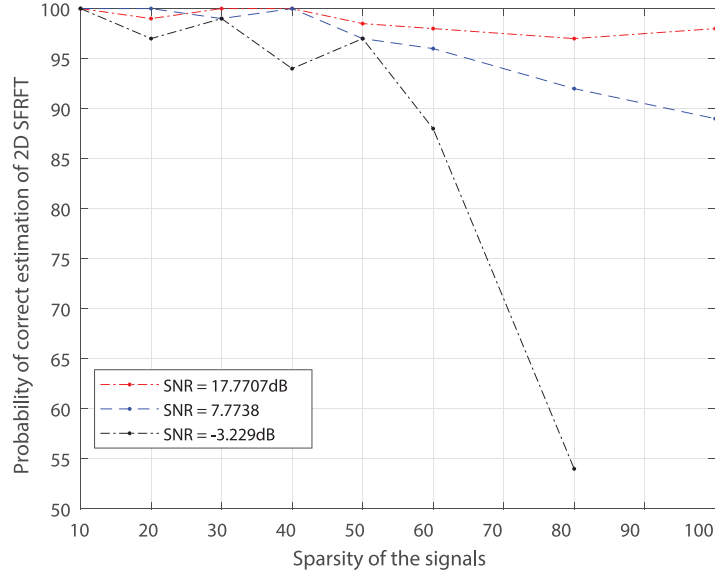

Fig. 6. Probability of all significant frequencies being estimated correctly.

$O(T(L \log L + L))$. Therefore, the runtime complexity of 2D SFRFT is $O(TL \log L + k)$.

For the case of noise, Step1 takes $O(L(T + sk))$ times complex multiplications and Step5 takes k times complex multiplications. For the iterative process, the inner loops are added. And the main cost of each inner loop is consumed in one FFT with runtime complexity $O(L \log L)$. And the running time complexity of the T iterative processes is $O(TL \log L + TL + skL \log L)$. Therefore, the runtime complexity of 2D SFRFT is $O((T + sk)L \log L)$.

5.4.3. Estimated probability

Without a doubt, the fractional Fourier spectrum can be fully estimated for the case of no noise. For the case of noise, Fig. 6 shows the probability of all significant frequency locations being estimated correctly. In this subsection, we will analyze the probability that the location (m_1, m_2) of one significant frequency is estimated correctly in the ith iteration. Assume that the number of remaining significant frequencies is k_i and the number of inner loops is $s < N_i n$ to estimate the location (m_1, m_2). First, this

frequency is required to pass the large-value bucket detection process in all of the $(3 + s)$ bucketing. And the probability of a large value bucket being detected correctly is not less than P_d (38). Second, the bucket m^1, which (m_1, m_2) is projected to during the first three bucketing, should be 1-sparse. If the locations of significant frequencies are uniformly distributed, the probability that one location has a significant frequency is $\frac{k_i}{N}$, where $N = N_1 N_2$. Hence, bucket m^1 is 1-sparse with probability $P_1 = (1 - \frac{k_i}{N})^{\frac{N}{L} - 1}$. Finally, the position error thresholds γ_1, γ_2 are large enough so that the true positions belong to the set of possible positions Υ_2. In summary, the probability of (m_1, m_2) being estimated correctly in the ith iteration is $P_d^{3+s} P_1 P_1^\gamma P_2^\gamma$ at least.

6. Application

In this section, to illustrate the effectiveness of the algorithm, we will implement parameter estimation of multicomponent 2D chirp signals, the fusion of multi-focused images, and parameters estimation for complex maneuvering targets in SAR radar.
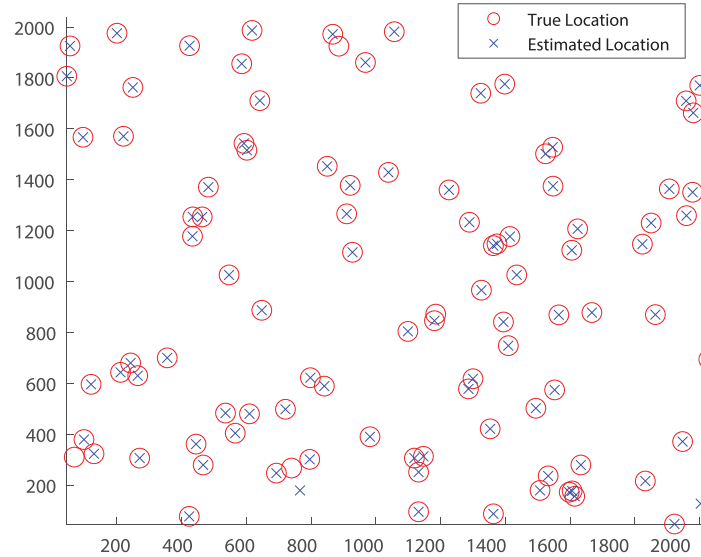
Fig. 7. Estimated Locations with SNR = −3.229 dB and $k = 100$.

6.1. Parameter estimation of multi-component two-dimensional chirp signals

In this subsection, we will perform parameter estimation on a three-component 2D chirp signal to verify the proposed algorithm's performance. Parameter estimation of 2D chirp signals is critical to statistical signal processing. The 2D chirp signals, i.e., quadratic polynomial phase signals, have been used in optical imaging, gray scale imaging, radar, sonar, and other fields widely. The mathematical model of multi-component 2D chirp signals is expressed as

$$f(s,t) = \sum_{l=1}^{c} A_l e^{j2\pi(f_l s + \frac{1}{2}\mu_l s^2 + \tilde{f}_l t + \frac{1}{2}\tilde{\mu}_l t^2)} \tag{50}$$

where c denotes the number of components. A_l denotes the magnitude of the lth component. $f_l, \tilde{f}_l$ are the center frequencies of the lth component. $\mu_l, \tilde{\mu}_l$ are the modulation frequencies of the lth component. For simplicity, in the simulation, the amplitudes A of the three 2D chirp components are equal to 0.5 and the modulation frequencies $(\mu, \tilde{\mu})$ are equal to $(-0.8, 0.24)$. And the sampling rate to discretize the continuous signal is equal to $2048 Hz/s$. The sampling has lasted for 0.0625 s and the contour map of the signal is displayed in Fig. 8(a). Fig. 8(b) shows the contour map of this signal with the addition of 4.587 dB Gaussian white noise.

On the one hand, we estimate the 2D DFT of the chirp signal by the MARS-SFT algorithm [54]. Due to the limitation of the Fourier transform, MARS-SFT cannot describe the characteristics of non-stationary signals completely. To be fair, the open-source code described in Wang et al. [54] is used. In detail, the threshold for frequency detection in a slice is set to 2×10^{-6}. The threshold for 1-sparse detection is also equal to 2×10^{-6}. The number of votes is chosen to be 3, and the vote threshold is 2. Then, the estimated result for Fig. 8(a) is shown in Fig. 9(a). The true center frequencies of three-component are (1088,416), (240,1600), and (1824,1632). By the MARS-SFT algorithm, the estimated center frequencies, that is, the positions of the significant frequencies, are (240,1552) and (1808,1616). A component is lost and the estimated components are shifted compared to the true center frequencies. In addition, the amplitudes have large errors too. For the noisy signal Fig. 8(b), the MARS-SFT algorithm doesn't work. Therefore, it is verified that the Fourier transform is not suitable for processing non-stationary signals.

On the other hand, we estimate the 2D DFRFT of the chirp signal by the robust 2D SFRFT algorithm with optimal rotation angles

$$(\alpha, \beta) = (\text{arccot}(-\mu), \text{arccot}(-\tilde{\mu})) \tag{51}$$

The fractional Fourier transform has a strong energy aggregation for chirp signals. And the robust 2D SFRFT can be used for both noiseless and noisy cases. In the simulation, the false alarm probability of large-value buckets detection is set to $P_{fa} = 0.001$. Meanwhile, the 1-sparse bucket detection threshold is $\delta = 200$. The row position error threshold γ_1 and the column position error threshold γ_2 are equal to 11. The number of iterations of the 2D SFRFT algorithm is taken as 1. During the simulation, the inner loop is executed 3 times. With $\sigma_1 = 95, \sigma_2 = 37, \tau_1 = 122, \tau_2 = 6$, the estimated result for Fig. 8(a) is shown in Fig. 9(b). By our method, the estimated center frequencies, that is, the positions of the three main frequencies are the same as the true center frequency exactly. In addition, the three amplitudes are estimated as 0.499991, 0.50007, and 0.49993, respectively. The error with the real amplitude of 0.5 is not more than 0.00007 for each component. For Fig. 8(b), the three bucketing results are shown in Fig. 10(a)–(c). Obviously, the three components are separated into different buckets. And the large-value buckets' positions have not changed with the translation of slices. The estimated result for Fig. 8(b) is shown in Fig. 10(d). The center frequencies of the three components are still correctly estimated. And the maximum amplitude error is 0.0194. In summary, the 2D SFRFT algorithm can estimate the center frequencies and magnitudes of multi-component 2D chirp signals accurately.

6.2. Parameters estimation for complex maneuvering targets in SAR radar

Synthetic aperture radar (SAR) is capable of all-weather imaging with high resolution and has been widely studied in both military and civilian applications [58,59]. We have studied SAR for the detection of uniformly accelerated moving targets [36]. In actual radar detection, complex maneuvering targets are much more common. In this section, we will utilize the symmetric correlation function and the proposed robust 2D SFRFT algorithm to estimate the motion parameters of the maneuvering target.
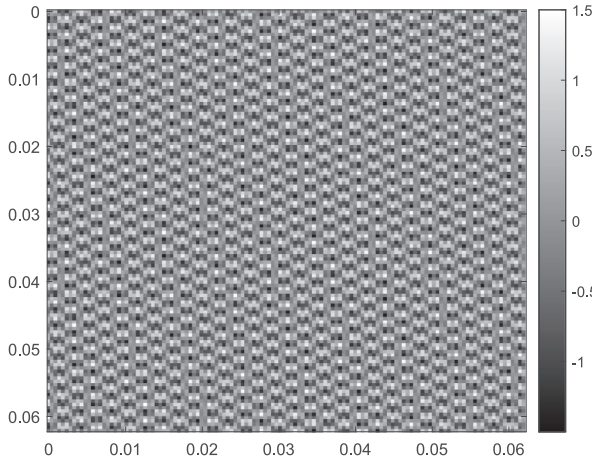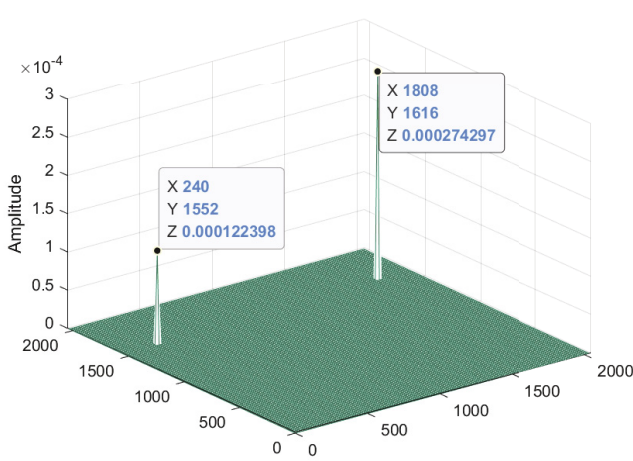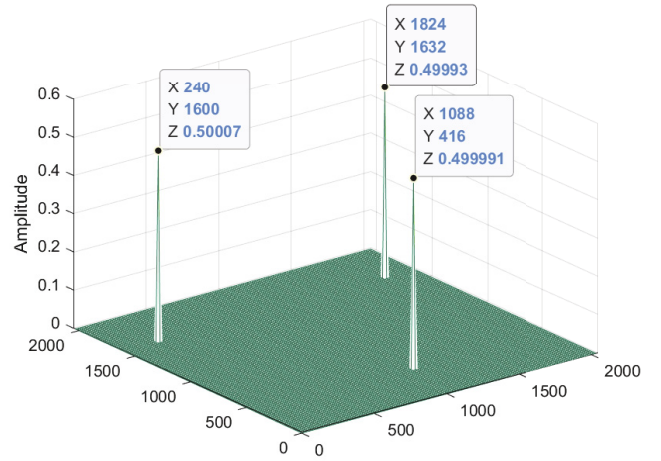
(a) The three-component chirp image without noise
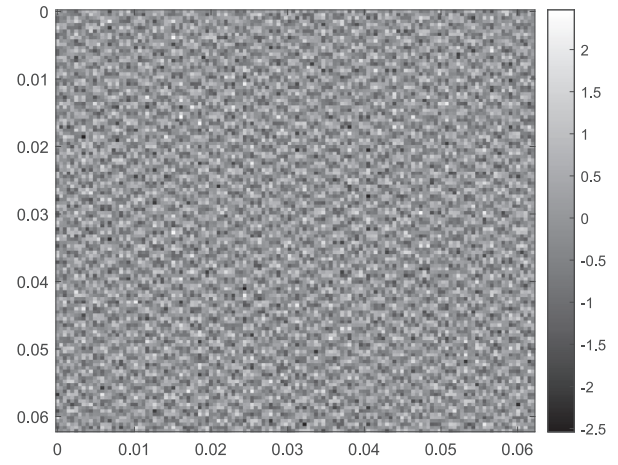
(b) The three-component chirp image with 4.587 dB Gaussian white noise.

Fig. 8. The three-component two-dimensional chirp signal.

(a) The estimated result of MARS-SFT [54] for Fig. 8(a).

(b) The estimated result of 2D SFRFT for Fig. 8(a).

Fig. 9. The estimated results for Fig. 8(a).

Assuming that the radar transmits linear modulated frequency pulses (LFM), which is denoted as

$$p(t) = rect\left(\frac{t}{T}\right)e^{j\pi(2f_c t + \mu t^2)} \tag{52}$$

where $rect()$ denotes rectangular window with

$$rect\left(\frac{t}{T}\right) = \begin{cases} 1, & |t| \le T/2 \\ 0, & |t| > T/2 \end{cases} \tag{53}$$

and T is the pulse bandwidth, $f_c = 6 \times 10^8$ Hz is the carrier frequency, and μ is the chirp rate. At the same time, the target is assumed to make a radial maneuvering motion relative to the radar. And the initial slope distance, radial velocity, acceleration, and jerk are expressed as R_0, v, a, g, separately. At any moment $t_m \in [-\frac{T_a}{2}, \frac{T_a}{2}]$, the instantaneous slant distance of the target can be approximated as Jin et al. [60]

$$R(t_m) \approx R_0 + v t_m + \frac{1}{2}a t_m^2 + \frac{1}{6}g t_m^3 \tag{54}$$

where $R_0 = 1486$ m, $v = -1.25$ m/s, $a = 6$ m/s^2, $g = 3$ m/s^3 are chosen to simulation. And $T_a = 4$ s denotes observation time. The

echo signal of the target can be expressed as

$$s(t_m) = Ae^{-j2\pi(a_1 t_m + a_2 t_m^2 + a_3 t_m^3)} \tag{55}$$

where A is the amplitude of $s(t_m)$. And $a_1 = \frac{2f_c v}{c}, a_2 = \frac{f_c a}{c}, a_3 = \frac{f_c g}{3c}$ are the coefficients to be estimated. c represents the speed of light, which is always take $c = 3 \times 10^8$ m/s. The real part of echo signal is shown in Fig. 11.

First of all, we calculate the symmetric correlation function of the echo signal, which is expressed as

$$Rx(t, \tau) = s(t + \tau)s^*(t - \tau)[s(t + \tau + \tau_0)s^*(t - \tau - \tau_0)]^* \tag{56}$$

$$= A^4 e^{j2\pi(2a_1\tau_0 + 2a_3\tau_0^3 + 4a_2\tau_0 t + 6a_3\tau_0 t^2 + 6a_3\tau_0^2\tau + 6a_3\tau_0\tau^2)} \tag{57}$$

where τ_0 is a fixed lag-time difference with $0 < \tau_0 < \frac{T_a}{4}$. We take $\tau_0 = 2$ in the simulation. The number of sampling points per dimension is 512 and the sampling frequency is taken as 128. It can be seen that $Rx(t, \tau)$ is a 2D chirp signal with center frequencies $(4a_2\tau_0, 6a_3\tau_0^2)$ and modulation frequencies $(6a_3\tau_0, 6a_3\tau_0)$. And with the proposed robust 2D SFRFT algorithm, we can estimate the parameters. Through experiments, we found that the energy of the
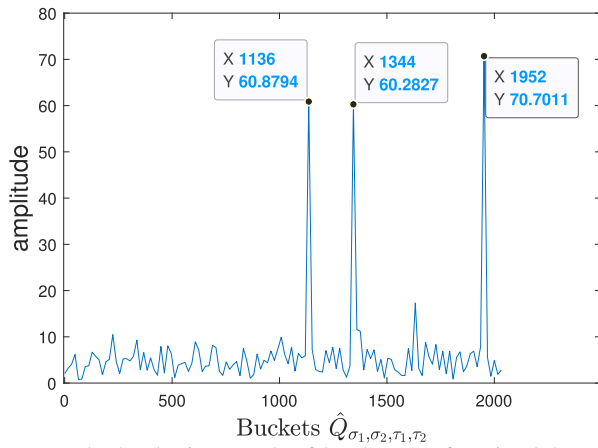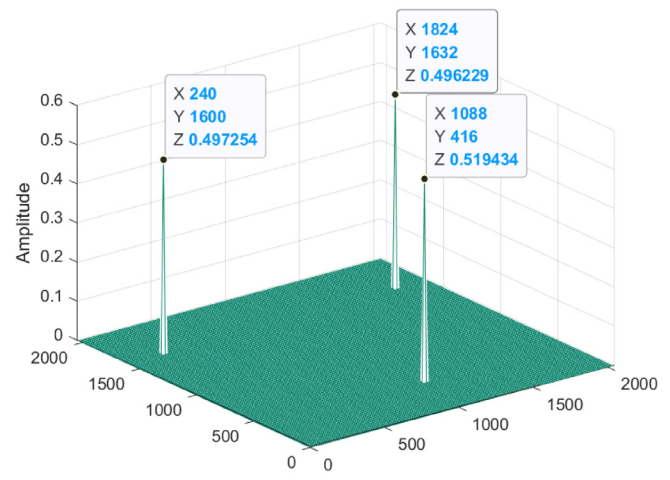
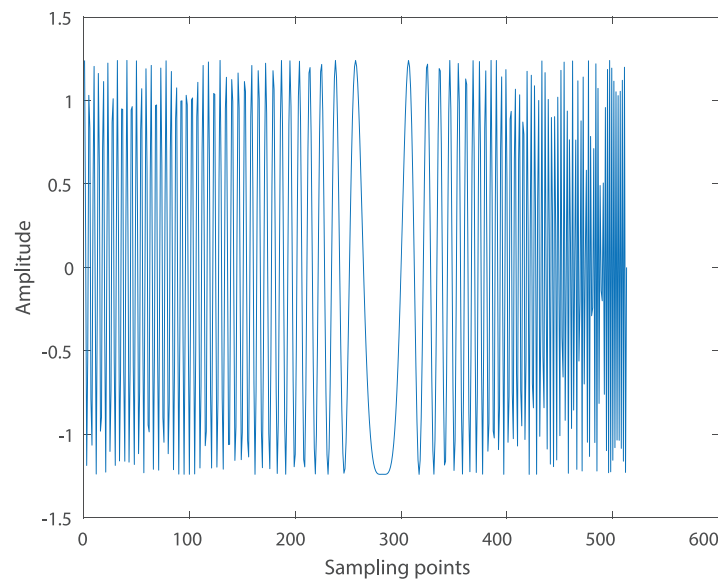(a) The bucketing result of 2D SFRFT for Fig. 8(b).
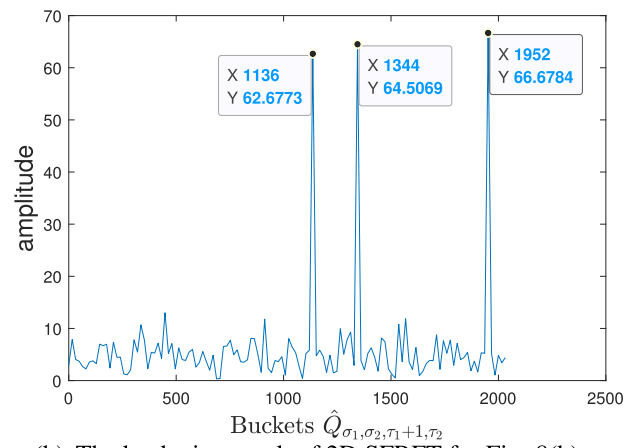
(b) The bucketing result of 2D SFRFT for Fig. 8(b).
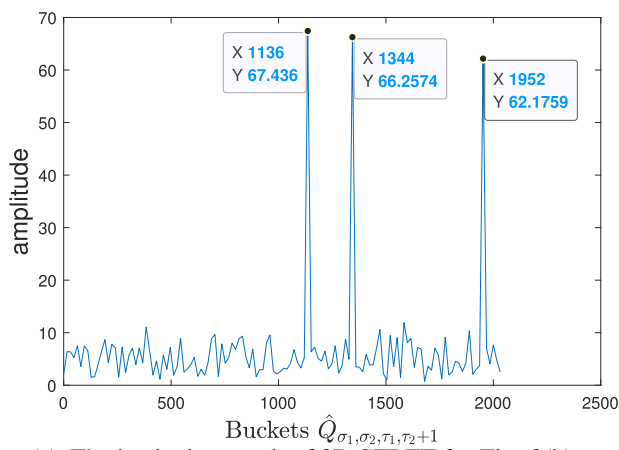
(c) The bucketing result of 2D SFRFT for Fig. 8(b).

(d) The estimated result of 2D SFRFT for Fig. 8(b).

Fig. 10. The estimated results for Fig. 8(b).

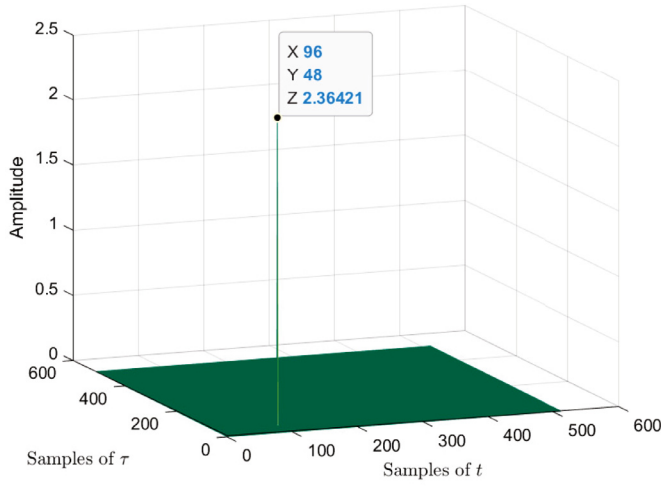**Fig. 11.** The real part of echo signal.

Fig. 12. The result estimated by robust 2D SFRFT algorithm.

signal is most aggregated when $\alpha = \beta = 1.9296$. And the indices of the significant frequency are (96,48). The corresponding estimation result is shown in Fig. 12. Therefore,

$$\begin{cases} 4a_2\tau_0 = 96 \\ 6a_3\tau_0^2 = 48 \end{cases} \tag{58}$$

Then, we can get $a_2 = 12$ and $a_3 = 2$. Accordingly, we obtain an estimate of the target acceleration $a = 6$ m/s^2 and an estimate of the jerk $g = 3$ m/s^3, which is consistent with actual parameters. Subsequently, we estimate $a_1 = -5$ by de-chirp technique and the FFT on $Rx(t, \tau)$. Thus, $v = -1.25$ m/s which is consistent with actual parameters too. Overall, we have accurately estimated the motion parameters of the complex maneuvering target.

6.3. Image fusion

In this subsection, we will use the robust 2D SFRFT algorithm to implement the fusion scheme. Image fusion is the combination of some images of an object into a new image. And the fused image can show the object more clearly. Image fusion processing is essential for remote sensing, medical images, and other fields. We use the robust 2D SFRFT algorithm to replace the 2D DFRFT in the image fusion scheme in Saxena and Sharma [39]. And Fig. 13 illustrates the flow of image fusion. Where images A and B are differently focused images of the same object. The details of the image can be extracted from the fractional Fourier spectrum by

$$E_A = A - |F_A| \tag{59}$$

$$E_B = B - |F_B| \tag{60}$$

In addition, ω_1, ω_2 are weights of the combination of AB and E_{AB}. And AB is obtained by maximum selection of image A and image B, which can be expressed as

$$AB(s, t) = \begin{cases} A(s, t), A(s, t) \geq B(s, t) \\ B(s, t), B(s, t) > A(s, t) \end{cases} \tag{61}$$

Similarly, E_{AB} is obtained by the maximum selection of image E_A and image E_B. To evaluate the clarity of fused images f numerically, the average gradient and spatial frequency are selected as evaluation metrics. The average gradient is defined as (62),

$$Ag(f) = \frac{1}{\sqrt{2}(N_1 - 1)(N_2 - 1)}$$
$$\times \sum_{i=0}^{N_1-2} \sum_{j=0}^{N_2-2} \sqrt{[f(i+1, j) - f(i, j)]^2 + [f(i, j+1) - f(i, j)]^2} \tag{62}$$

and its larger value indicates more detail in the image. The spatial frequency is defined as (63),

$$Sf(f) = \sqrt{\frac{1}{N_1 N_2} \left\{ \sum_{i=0}^{N_1-1} \sum_{j=1}^{N_2-1} [f(i, j) - f(i, j-1)]^2 + \sum_{i=1}^{N_1-1} \sum_{j=0}^{N_2-1} [f(i, j) - f(i-1, j)]^2 \right\}} \tag{63}$$

and its larger value indicates a higher quality of the image.

This image fusion scheme is implemented in the Multi-focus Image Fusion Dataset master and partial results are shown in Fig. 14. Where, the rows are grayscale images of boats, crossroad, building, and peoples, respectively. The first and second columns are the multi-focused images used for the simulation, and the third column is our fused image. In addition, the average gradients and spatial frequencies of the fused images are shown in Table 4. The parts of the original images that are clear remain clear after fusion. And the blurred parts of the original images become clearer after fusion.

7. Conclusion

In this paper, we explore the robust 2D SFRFT algorithm in theory and applications. First of all, a low-complexity 2D SFRFT algorithm for noiseless signals is proposed. Then, based on the analysis of noises, the spectral estimation method for noisy signals is proposed. Finally, algorithm performance simulations and applications are given. Compared with the decomposition and Pei method, 2D FRFT is optimal in terms of efficiency and accuracy, regardless of signal sizes. The simulation also shows that the position error threshold is independent of the location of the significant frequency and increases with the growth of the position probability and noises. In addition, we verify that the robust 2D SFRFT is convergent. The significant frequencies can be recovered with a high probability by a few iterations and inner loops. The sample
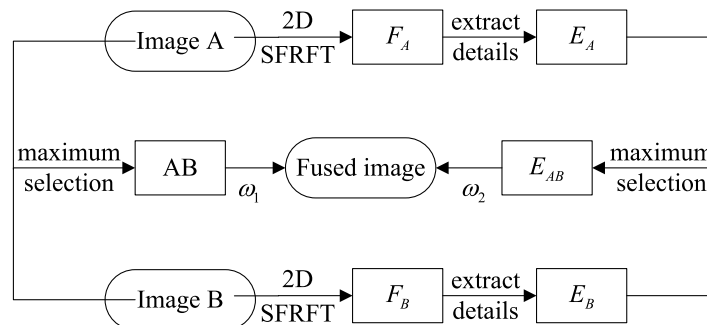

Fig. 13. Image fusion flow.

(a) Boats A.

(b) Boats B.

(c) Boats fusion.

(d) Crossroad A.

(e) Crossroad B.

(f) Crossroad fusion.

(g) Building A.

(h) Building B.

(i) Building fusion.

(j) People A.

(k) People B.

(l) People fusion.

Fig. 14. Image fusion by robust 2D SFRFT algorithm.

Table 4
The clarity evaluation of fused images.

Fused image	Boats	Crossroad	Building	People
Average gradient	3.2239 − 0.0001i	11.0887 + 0.0003i	7.5737 − 0.0001i	6.5474 + 0.0004i
Spatial frequency	10.586 − 0.0041i	37.4298 + 0.0010i	24.4533 − 0.0004i	18.6519 + 0.0012i

complexity, runtime complexity, and probabilities of the algorithms are analyzed in detail. 2D SFRFT estimates the center frequency and amplitude of a multicomponent chirp signal accurately, which 2D SFT [54] cannot realize. In addition, robust 2D SFRFT is performed for image fusion successfully. The estimation of parameters for complex maneuvering targets in SAR radar is also realized. In future research, we would like to apply the robust 2D SFRFT algorithm to the parameter estimation of optical components. Sparse-based fast algorithms for others 2D DFRFT and linear canonical transformation are also a good research direction.

Declaration of Competing Interest

The authors declare that they have no known competing financial interests or personal relationships that could have appeared to influence the work reported in this paper.

CRediT authorship contribution statement

Deyun Wei: Conceptualization, Formal analysis, Funding acquisition, Methodology, Writing – review & editing. **Jun Yang:** Conceptualization, Data curation, Formal analysis, Investigation, Software, Validation, Writing – original draft.

Acknowledgment

References

[1] M. Zubair, S. Ahmed, M.-S. Alouini, Frequency diverse array radar: new results and discrete Fourier transform based beampattern, IEEE Trans. Signal Process. 68 (2020) 2670–2681.

[2] D. Wei, Q. Ran, Y. Li, J. Ma, L. Tan, Fractionalisation of an odd time odd frequency DFT matrix based on the eigenvectors of a novel nearly tridiagonal commuting matrix, IET Signal Process. 5 (2) (2011) 150–156.

[3] D. Wei, Y. Li, Novel tridiagonal commuting matrices for types I, IV, V, VIII DCT and DST matrices, IEEE Signal Process. Lett. 21 (4) (2014) 483–487.

[4] H.W. Levinson, V.A. Markel, Binary discrete Fourier transform and its inversion, IEEE Trans. Signal Process. 69 (2021) 3484–3499.

[5] S. Zhu, G. Liao, D. Yang, H. Tao, A new method for radar high-speed maneuvering weak target detection and imaging, IEEE Geosci. Remote Sens. Lett. 11 (7) (2013) 1175–1179.

[6] M. Kronauge, H. Rohling, New chirp sequence radar waveform, IEEE Trans. Aerosp. Electron. Syst. 50 (4) (2014) 2870–2877.

[7] B.P. Abbott, R. Abbott, T. Abbott, M. Abernathy, F. Acernese, K. Ackley, C. Adams, T. Adams, P. Addesso, R. Adhikari, et al., Observation of gravitational waves from a binary black hole merger, Phys. Rev. Lett. 116 (6) (2016) 061102.

[8] H.M. Ozaktas, Z. Zalevsky, M.A. Kutay, The Fractional Fourier Transform with Applications in Optics and Signal Processing, Wiley, 2001.

[9] A. Zayed, Two-dimensional fractional Fourier transform and some of its properties, Integral Transf. Spec. Funct. 29 (7) (2018) 553–570.

[10] Y. Liu, H. Miao, F. Zhang, R. Tao, Sliding 2D discrete fractional Fourier transform, IEEE Signal Process. Lett. 26 (12) (2019) 1733–1737.

[11] J.J. Healy, M.A. Kutay, H.M. Ozaktas, J.T. Sheridan, Linear Canonical Transforms: Theory and Applications, Springer, 2016.

[12] L. Qi, R. Tao, S. Zhou, Y. Wang, Detection and parameter estimation of multicomponent LFM signal based on the fractional Fourier transform, Sci. China Ser. F 47 (2) (2004) 184–198.

[13] L.B. Almeida, The fractional Fourier transform and time-frequency representations, IEEE Trans. Signal Process. 42 (11) (1994) 3084–3091.

[14] S. Xu, L. Feng, Y. Chai, Y. He, Analysis of a-stationary random signals in the linear canonical transform domain, Signal Process. 146 (2018) 126–132.

[15] Z. Zhang, Linear canonical Wigner distribution based noisy LFM signals detection through the output SNR improvement analysis, IEEE Trans. Signal Process. 67 (21) (2019) 5527–5542.

[16] M.R. Abuturab, A. Alfalou, Multiple color image fusion, compression, and encryption using compressive sensing, chaotic-biometric keys, and optical fractional Fourier transform, Opt. Laser Technol. 151 (2022) 108071.

[17] C. Zhang, J. Shi, Z. Zhang, Y. Liu, X. Hu, FRFT-based interference suppression for OFDM systems in IoT environment, IEEE Commun. Lett. 23 (11) (2019) 2068–2072.

[18] H. Xin, X. Bai, Y. Song, B. Li, R. Tao, ISAR imaging of target with complex motion associated with the fractional Fourier transform, Digit. Signal Process. 83 (2018) 332–345.

[19] E. Sejdić, I. Djurović, L. Stanković, Fractional Fourier transform as a signal processing tool: an overview of recent developments, Signal Process. 91 (6) (2011) 1351–1369.

[20] A. Kumar Singh, R. Saxena, Recent developments in FRFT, DFRFT with their applications in signal and image processing, Recent Pat. Eng. 5 (2) (2011) 113–138.

[21] Z. Zhang, New Wigner distribution and ambiguity function based on the generalized translation in the linear canonical transform domain, Signal Process. 118 (2016) 51–61.

[22] D. Wei, Y. Li, Generalized sampling expansions with multiple sampling rates for lowpass and bandpass signals in the fractional Fourier transform domain, IEEE Trans. Signal Process. 64 (18) (2016) 4861–4874.

[23] D. Wei, Y. Li, Convolution and multichannel sampling for the offset linear canonical transform and their applications, IEEE Trans. Signal Process. 67 (23) (2019) 6009–6024.

[24] D. Wei, Q. Ran, Y. Li, Generalized sampling expansion for bandlimited signals associated with the fractional Fourier transform, IEEE Signal Process. Lett. 17 (6) (2010) 595–598.

[25] X. Su, R. Tao, X. Kang, Analysis and comparison of discrete fractional Fourier transforms, Signal Process. 160 (2019) 284–298.

[26] J.R. de Oliveira Neto, J.B. Lima, Discrete fractional Fourier transforms based on closed-form Hermite–Gaussian-like DFT eigenvectors, IEEE Trans. Signal Process. 65 (23) (2017) 6171–6184.

[27] J.R. de Oliveira Neto, J.B. Lima, G.J. da Silva Jr., R.M.C. de Souza, Computation of an eigendecomposition-based discrete fractional Fourier transform with reduced arithmetic complexity, Signal Process. 165 (2019) 72–82.

[28] C. Candan, M.A. Kutay, H.M. Ozaktas, The discrete fractional Fourier transform, IEEE Trans. Signal Process. 48 (5) (2000) 1329–1337.

[29] Y. Sun, B. Li, Sliding discrete linear canonical transform, IEEE Trans. Signal Process. 66 (17) (2018) 4553–4563.

[30] H.M. Ozaktas, O. Arikan, M.A. Kutay, G. Bozdagt, Digital computation of the fractional Fourier transform, IEEE Trans. Signal Process. 44 (9) (1996) 2141–2150.

[31] S. Pei, J. Ding, Closed-form discrete fractional and affine Fourier transforms, IEEE Trans. Signal Process. 48 (5) (2000) 1338–1353.

[32] S. Liu, T. Shan, R. Tao, Y.D. Zhang, G. Zhang, F. Zhang, Y. Wang, Sparse discrete fractional Fourier transform and its applications, IEEE Trans. Signal Process. 62 (24) (2014) 6582–6595.

[33] H. Zhang, T. Shan, S. Liu, R. Tao, Optimized sparse fractional Fourier transform: principle and performance analysis, Signal Process. 174 (2020) 107646.

[34] X. Yu, X. Chen, Y. Huang, J. Guan, Sparse fractional Fourier transform and its applications in radar moving target detection, in: 2018 International Conference on Radar (RADAR), IEEE, 2018, pp. 1–5.

[35] X. Yu, X. Chen, Y. Huang, J. Guan, Fast detection method for low-observable maneuvering target via robust sparse fractional Fourier transform, IEEE Geosci. Remote Sens. Lett. 17 (6) (2019) 978–982.

[36] D. Wei, H. Hu, Sparse discrete linear canonical transform and its applications, Signal Process. 183 (2021) 108046.

[37] D. Wei, Y. Shen, Fast numerical computation of two-dimensional non-separable linear canonical transform based on matrix decomposition, IEEE Trans. Signal Process. 69 (2021) 5259–5272.

[38] S. Pei, M. Yeh, Two dimensional discrete fractional Fourier transform, Signal Process. 67 (1) (1998) 99–108.

[39] N. Saxena, K. Sharma, Image fusion scheme using two dimensional discrete fractional Fourier transform, in: 2017 Conference on Information and Communication Technology, IEEE, 2017, pp. 1–6.

[40] M.A. Kutay, H.M. Ozaktas, Optimal image restoration with the fractional Fourier transform, JOSA A 15 (4) (1998) 825–833.

[41] N. Saxena, K.K. Sharma, Pansharpening scheme using filtering in two-dimensional discrete fractional Fourier transform, IET Image Process. 12 (6) (2018) 1013–1019.

[42] R. Tao, X. Meng, Y. Wang, Image encryption with multiorders of fractional Fourier transforms, IEEE Trans. Inf. Forensics Secur. 5 (4) (2010) 734–738.

[43] Y. Guo, B. Li, Blind image watermarking method based on linear canonical wavelet transform and QR decomposition, IET Image Process. 10 (10) (2016) 773–786.

[44] Q. Shi, W. Li, R. Tao, X. Sun, L. Gao, Ship classification based on multifeature ensemble with convolutional neural network, Remote Sens. 11 (4) (2019) 419.

[45] A.D. Algarni, G. El Banby, S. Ismail, W. El-Shafai, F.E.A. El-Samie, N. F Soliman, Discrete transforms and matrix rotation based cancelable face and fingerprint recognition for biometric security applications, Entropy 22 (12) (2020) 1361.

[46] H. Hassanieh, P. Indyk, D. Katabi, E. Price, Simple and practical algorithm for sparse fourier transform, in: Proceedings of the 2012 Annual ACM-SIAM Symposium on Discrete Algorithms, 2012, pp. 1183–1194.

[47] H. Hassanieh, P. Indyk, D. Katabi, E. Price, Nearly optimal sparse fourier transform, in: Proceedings of the Forty-Fourth Annual ACM Symposium on Theory of Computing, 2012, pp. 563–578.

[48] H. Haitham, The sparse Fourier transform: theory and practice, Association for Computing Machinery and Morgan & Claypool, ACM Books, 2018.

[49] H. Ghani, M.R.A. Malek, M.F.K. Azmi, M.J. Muril, A. Azizan, A review on sparse fast Fourier transform applications in image processing, Int. J. Electr. Comput. Eng. 10 (2) (2020) 1346–1351.

[50] H. Zhang, T. Shan, S. Liu, R. Tao, Performance evaluation and parameter optimization of sparse Fourier transform, Signal Process. 179 (2021) 107823.

[51] B. Ghazi, H. Hassanieh, P. Indyk, D. Katabi, E. Price, L. Shi, Sample-optimal average-case sparse Fourier transform in two dimensions, in: 2013 51st Annual Allerton Conference on Communication, Control, and Computing (Allerton), IEEE, 2013, pp. 1258–1265.

[52] H. Hassanieh, M. Mayzel, L. Shi, D. Katabi, V.Y. Orekhov, Fast multi-dimensional NMR acquisition and processing using the sparse FFT, J. Biomol. NMR 63 (1) (2015) 9–19.

[53] D. Potts, T. Volkmer, Sparse high-dimensional FFT based on rank-1 lattice sampling, Appl. Comput. Harmon. Anal. 41 (3) (2016) 713–748.

[54] S. Wang, V.M. Patel, A. Petropulu, Multidimensional sparse Fourier transform based on the Fourier projection-slice theorem, IEEE Trans. Signal Process. 67 (1) (2018) 54–69.

[55] S. Wang, V.M. Patel, A. Petropulu, The robust sparse Fourier transform (RSFT) and its application in radar signal processing, IEEE Trans. Aerosp. Electron. Syst. 53 (6) (2017) 2735–2755.

[56] M. Kapralov, A. Velingker, A. Zandieh, Dimension-independent sparse Fourier transform, in: Proceedings of the Thirtieth Annual ACM-SIAM Symposium on Discrete Algorithms, SIAM, 2019, pp. 2709–2728.

[57] P. Viswanath, D.N.C. Tse, R. Laroia, Opportunistic beamforming using dumb antennas, IEEE Trans. Inf. Theory 48 (6) (2002) 1277–1294.

[58] A. Freeman, SAR calibration: an overview, IEEE Trans. Geosci. Remote Sens. 30 (6) (1992) 1107–1121.

[59] A. Moreira, P. Prats-Iraola, M. Younis, G. Krieger, I. Hajnsek, K.P. Papathanassiou, A tutorial on synthetic aperture radar, IEEE Geosci. Remote Sens. Mag. 1 (1) (2013) 6–43.

[60] K. Jin, H. Zhang, Y. Wang, Z. Han, Y. Zhao, Coarse-to-fine coherent integration method for radar maneuvering target with complex motion, J. Appl. Remote Sens. 13 (3) (2019) 036507.

[61] J. Yang, J. Shen, Sparse signal detection and fingerprint feature recognition based on fast 2D DFRFT, in: 2022 3rd Information Communication Technologies Conference, (ICTC), 2022, pp. 146–150.